Published in final edited form as:

Nat Methods. 2022 November ; 19(11): 1490–1499. doi:10.1038/s41592-022-01650-9.

CODA: Quantitative 3D reconstruction of large tissues at cellular resolution

Ashley Kiemen[1], **Alicia M. Braxton**[2], **Mia P. Grahn**[1], **Kyu Sang Han**[1], **Jaanvi Mahesh Babu**[2], **Rebecca Reichel**[2], **Ann C. Jiang**[3], **Bridgette Kim**[4], **Jocelyn Hsu**[1], **Falone Amoa**[2], **Sashank Reddy**[5], **Seung-Mo Hong**[6], **Toby C. Cornish**[7], **Elizabeth D. Thompson**[2], **Peng Huang**[8,9], **Laura D. Wood**[2,9], **Ralph H. Hruban**[2,9], **Denis Wirtz**[1,2,9,10,11,*], **Pei-Hsun Wu**[1,*]

[1]Department of Chemical and Biomolecular Engineering, The Johns Hopkins University; 3400 N Charles St, Baltimore, Maryland 21218, USA

[2]Department of Pathology, The Sol Goldman Pancreatic Cancer Research Center, The Johns Hopkins University School of Medicine; 1800 Orleans St, Baltimore, Maryland 21287, USA

[3]Department of Biomedical Engineering, The Johns Hopkins University; 3400 N Charles St, Baltimore, Maryland 21218, USA

[4]Department of Mechanical Engineering, The Johns Hopkins University; 3400 N Charles St, Baltimore, Maryland 21218, USA

[5]Department of Plastic and Reconstructive Surgery, The Johns Hopkins University School of Medicine; 1800 Orleans St, Baltimore, Maryland 21287, USA

[6]Department of Pathology, Asan Medical Center, University of Ulsan College of Medicine; 88, Olympic-ro 43 gil, Seoul, 05505, Republic of Korea

[7]Department of Pathology, University of Colorado School of Medicine; 13001 E 17th Pl, Aurora, CO 80045, USA

[8]Department of Biostatistics, The Johns Hopkins University; 3400 N Charles St, Baltimore, Maryland 21218, USA

[9]Department of Oncology, The Johns Hopkins University School of Medicine; 1800 Orleans St, Baltimore, Maryland 21287, USA

[*]Corresponding authors: Denis Wirtz (wirtz@jhu.edu) and Pei-Hsun Wu (pwu@jhu.edu).

Author contributions:
Conceptualization: LDW, RHH, PHW, DW.
Image registration methodology: PHW, ALK.
Deep learning methodology: ALK.
3D reconstruction methodology: ALK.
3D quantification methodology: PHW, ALK.
CODA Validation: AJ, PHW, ALK.
Collagen alignment methodology: PHW, KSH, ALK.
Tissue annotation: MPG, AMB, JMB, RR, FA, ALK, AJ, BK, JH.
Tissue collection, sectioning, & scanning: TCC, AMB.
Pathology consultation: SMH, EDT, LDW, RHH.
Biostatistics calculations: ALK, PHW, PH.
Writing – original draft ALK, PHW, DW.
Writing – review & editing: DW, PHW, LDW, RHH, PH, MPG, AMB, JMB, RR, FA, AJ, BK, JH, KSH, SMH, EDT, TCC, ALK.

Competing interests: Authors declare that they have no competing interests.

[10]Department of Materials Science and Engineering, The Johns Hopkins University; 3400 N Charles St, Baltimore, Maryland 21218, USA

[11]Johns Hopkins Physical Sciences - Oncology Center, The Johns Hopkins University; 3400 N Charles St, Baltimore, Maryland 21218, USA

Abstract

A central challenge in biology is obtaining high-content, high-resolution information while analyzing tissue samples at volumes relevant to disease progression. We address this here with CODA, a method to reconstruct exceptionally large (up to multi centimeter cube) tissues at subcellular resolution using serially sectioned hematoxylin and eosin-stained tissue sections. Here we demonstrate CODA's ability to reconstruct in 3D distinct microanatomical structures in pancreas, skin, lung, and liver tissues. Importantly, CODA allows creation of readily quantifiable tissue volumes amenable to biological research. As a testbed, we assess the microanatomy of the human pancreas during tumorigenesis within the branching pancreatic ductal system, labelling ten distinct structures to examine heterogeneity and structural transformation during neoplastic progression. We show that pancreatic precancerous lesions develop into distinct 3D morphological phenotypes and that pancreatic cancer tends to spread far from the bulk tumor along collagen fibers that are highly aligned to the 3D curves of ductal, lobular, vascular, and neural structures. CODA establishes a means to transform broadly the structural study of human diseases through exploration of exhaustively labelled 3D microarchitecture.

One Sentence Summary:

Here we introduce and validate CODA, a powerful tool for 3D quantification of serially sectioned tissue, through reconstruction of human and murine tissues.

The growth of invasive cancer and its spread into microenvironments containing complex vascular, neural, stromal, and ductal structures is best understood through accurate three dimensional (3D) representations[1,2]. Pancreatic ductal adenocarcinoma (PDAC) is one of the deadliest forms of cancer, with a 5-year survival rate of only 10%[3,4]. PDAC arises from well-characterized precursor lesions in the pancreatic ducts and has a propensity for metastasis to the liver, lymph nodes, and retroperitoneum, often facilitated by vascular and neural invasion[5–7]. These phenomena are classically studied in two dimensions (2D) via tissue sectioning and histological staining, where 3D information such as connectivity, morphology, and spatial relationships are lost. While many surrogates for studying tumorigenesis have been developed *in vitro* and *in vivo*[8–12], quantitative 3D study of naturally occurring cancers in human tissues, or cancer *in situ*, is generally lacking.

Recent advances in tissue clearing techniques have been employed to explore human diseases in 3D[13–19]. Clearing of human pancreatic samples has been used to study the expression of a limited number of proteins in cancer cells as they invade into blood vessels[2] and to enumerate the density of islets of Langerhans[20]. However, poor antibody penetration into dense tissues such as PDAC's desmoplastic stroma requiring processing times of days to weeks, a trade-off between reconstruction of large volumes and number of structures labelled, and longstanding challenges in quantifying complex 3D images hinder the power

of tissue clearing techniques[15,18,21]. Reconstruction of serial hematoxylin and eosin (H&E) stained sections using image registration approaches has also been used to study disease in 3D[22–27]. While utilization of thinly stained sections avoids the issue of poor antibody penetration seen in study of intact tissues, time-consuming manual annotations and costly immunohistochemical (IHC) labeling and mass spectrometry have been required to identify components in serially sectioned specimens[23,24].

Here, we introduce CODA: a novel method for effective 3D reconstruction of large tissues from serially sectioned H&E images. We present the first fully integrated pipeline for labelled, 3D reconstruction of serial tissue images at single cell resolution with detailed comparison to existing methodologies. While previous techniques exist for registration[25,26], cell detection[28,29], and tissue multi-labelling in H&E images[30,31], we show that our integrated approach allows rapid, consistent reconstruction of serial samples from organs such as pancreas, skin, lung, and liver.

To demonstrate CODA's utility in microanatomical research, we explore 3D modes of pancreas tumorigenesis. We analyzed 4,114 H&E sections to reconstruct thirteen samples of up to 3.5cm^3 comprising normal, precancerous, and cancerous human pancreas at subcellular resolution. With deep learning semantic segmentation, we label ten distinct cell and tissue types without incorporation of additional stains. The power of CODA is demonstrated through visualization of complex pancreatic ductal morphology; characterization of the extent, 3D structure, and cellularity of pancreatic precursors; quantification of fiber alignment in a 3D landscape; and exploration of structures utilized by pancreatic cancer to invade far from the bulk tumor.

Results

CODA: 3D reconstruction of serial histological sections

To develop CODA, a method for the 3D reconstruction of serially sectioned tissue, we identified fourteen human pancreas samples (designated samples P0 – P13) containing normal pancreatic parenchyma, pancreatic parenchyma with precancerous lesions, and untreated invasive pancreatic cancer, as detailed in Table S1. Sample P0 contains 101 serial images sampled 4μm apart and was used only to optimize the workflow. Thick formalin-fixed paraffin-embedded samples were sectioned, stained with H&E, and digitized at 20x magnification, providing x and y (lateral) resolution of 0.5μm and z (axial) resolution of 4μm (Fig 1a).

First, the independent serial images were mapped to a common coordinate system using a novel image registration approach (Fig 1b). Images were coarsely aligned using whole field rigid-body registration, followed by an elastic registration approach to account for local tissue warping, similar to previously developed workflows[23–25,32–34]. The method serially aligned the 101 serial histological sections in P0 in 30 minutes (Extended Data Fig 1, detailed processing time estimates in Table S2). Importantly, to limit accumulation of error due to imperfect tissue sectioning, our algorithm is designed to discard registration to badly deformed tissues (containing large regions of splitting or folding).

Next, we established a high throughput H&E cell detection workflow based on color deconvolution and normalization and a previously established algorithm for particle tracking[35] intended for rapid cell detection in large serially sectioned samples without the need for training or manual annotations. CODA cell detection delivers a processing time of approximately 90 seconds per whole slide image (Fig 1c, Extended Data Fig 2).

We established a deep learning workflow for semantic segmentation of histological features and used it to identify nine pancreatic cell and tissue components in H&E: normal ductal epithelium, pancreatic cancer precursors, PDAC, smooth muscle, acini, fat, collagen, islets of Langerhans, and lymph nodes (Fig 1d, Extended Data Fig 3). The pipeline used DeepLab semantic segmentation and a pretrained ResNet50 network[36], achieved class precision and recall of >90% per sample (Extended Data Fig 4a), and labelled images to a resolution of 2μm/pixel in under three minutes each (computer specifications in Table S2). Our workflow allows segmentation of more pancreas tissues than previously developed methods[31] and is amenable to rapid (~1 day) generation of functional models. As sample collection was staggered, individual deep learning models were created for each sample. To demonstrate the ability of CODA to label additional structures in samples after creation of the first model, a second model was trained on all thirteen samples to identify nerves in the pancreas, with precision and recall >90% (Extended Data Fig 4b).

Validation of CODA methodology

We compared our registration approach to seven other methods using data in a previously published comparative analysis of tissue registration algorithms[34] and found that CODA registration outperforms the other techniques particularly in limiting the accumulation of error across large samples and maintains higher pixel correlation between images (Fig 2a).

To validate cell detection accuracy and compare to pre-existing techniques, five randomly selected 1.5 mm^2 image tiles were manually annotated by two researchers. Manual annotations were compared to CODA cell detection as well as two commonly used approaches.[28,29] CODA cell detection achieved the highest overall accuracy of the three techniques assessed with >90% precision and recall (Extended Data Fig 4c), and, importantly for assessment of samples containing many serial samples, CODA cell detection was on average 3-fold faster than the other techniques (Extended Data Fig S2a). *In situ* diameters of each cell type were measured and incorporated to extrapolate 3D cell counts from cell counts on serial 2D images (Extended Data Fig S2b).

We additionally assessed the effect of reducing the z-resolution of the samples by registering a subset of serial images. We found that registration performed with 95% similarity between consecutive sections or sections up to five axial planes apart (Fig 2b). Further, we found that we maintained 96% accuracy in estimation of cell count and tissue content by interpolating 3D cell count and deep learning labels from sections up to three axial planes apart (Fig 2c, 2d). This allowed us to improve workflow throughput by processing only one in three serial images in samples P1-P13 for an axial resolution of 12μm. We next confirmed the quality of 3D renderings by creating visualizations of a region of the pancreatic ductal architecture from sample P0 at z-resolutions of 4, 12, 48, and 96μm (Fig. 2e).

Finally, to demonstrate the ability of CODA to reconstruct non-pancreatic structures, we assessed samples of human scalp (Fig. 3a), murine lung (Fig. 3b), and murine liver (Fig 3c). CODA was used to label six structures in skin, five structures in lung, and four structures in liver, and to create detailed renderings of a range of tissue microanatomy.

Exploration of pancreas tumorigenesis in 3D

To demonstrate the utility of CODA for biological research, we created multi-labeled 3D maps of thirteen resected pancreas tissue samples of volumes up to 3.5cm^3 and containing up to 1.6 billion cells (Fig 4a). Eight of the samples assessed contained regions of grossly normal pancreatic parenchyma (sample P1 — P4, P6 — P9), nine contained pancreatic precursor lesions (sample P2 — P10), and eight contained regions of invasive pancreatic cancer (sample P6 — P13). We created multi-scale renderings that demonstrate the complex, curved architecture of the normal pancreatic ducts and periductal collagen, the surrounding acinar lobules, islets of Langerhans, fat, and blood vessels (Movies S1–S6).

Through quantification of tissue volume and cell count, we investigated the compositional changes to the pancreas during tumorigenesis. We compared the volume and cell composition of tissue components in the samples (Table S3). Our results revealed an average 2.3 fold decrease in cell density between healthy regions and invasive cancer regions in the pancreas with a p-value of $<10^{-4}$ using the Wilcoxon rank sum test (Fig 4b). At the extreme end, we found zero acinar tissue and an astonishing 87% collagen composition in sample P11, a 14-fold increase from normal pancreas architecture, emphasizing the scale of atrophy, dense desmoplastic stroma, and tissue reorganization brought with pancreatic cancer.

Microarchitectural properties of pancreatic precancers

Following bulk assessment of the samples, we utilized CODA to enumerate architectural patterns of pancreatic precursor lesions in 3D. Of the thirteen samples analyzed, eight contained pancreatic intraepithelial neoplasia (PanIN) and one contained intraductal papillary mucinous neoplasms (IPMNs). PanIN are clinically defined as mucin-producing epithelial neoplasms residing in ducts <0.5cm, with larger neoplasms typically denoted as IPMNs and both involve the complex tubular branches of the pancreatic ducts and “bunches of grape-like” acinar lobules[37]. It is currently not possible to noninvasively detect the smallest of these lesions in the clinic[38–40]. Here we present insights into pancreatic precancers of volumes that are undetectable using clinical approaches (0.0005 – 30 mm^3) that may inform the design of novel detection tests.

We found that precursors occupy a range of volumes, can be simple or highly branched, and may be densely packed yet unconnected in 3D. Using the 3D reconstruction of the ductal system of sample P2, we identified 43 spatially independent precancers in a 2.3cm^3 sample (Fig 5a, Movie S7). In one section, a large precursor was identified in multiple ducts separated by nearly 1cm and surrounded by multiple, smaller precursors exemplifying how connectivity is difficult to interpret from 2D alone. In the nine samples containing precursors (samples P2-P10), we compared the number of distinct precursors per section with and without considering 3D connectivity and found that 2D lesion number over-counted the true 3D tumor number per section by as much as a factor of 40, exemplifying the complex

3D connectivity of pancreatic precancers (Fig 5b). This measurement yielded an average 12.3-fold overcounting in 2D vs 3D with a p-value of $<10^{-5}$ using a Wilcoxon rank sum test.

While assessing 3D connectivity of the precursors, we identified three distinct 3D structural phenotypes which we term tubular, lobular, and dilated (Fig 5c, Movie S8). Tubular precancers appeared as ductal, branching structures, dilated precancers appeared as large ballooning of the duct connected to ducts of much smaller diameters, and lobular precancers appeared as "bunches of grape-like," connected locules forming a nodule. Review of the corresponding H&E sections by pancreatic pathologists revealed that tubular PanINs resided within pancreatic ducts, dilated PanINs resided within regions of dilated pancreatic ducts, and lobular PanINs resided at the terminal junctions of ducts and acinar lobules, involving areas of acinar to ductal metaplasia (ADM)[41,42]. These phenotypes appear similar to pancreatic precancer phenotypes identified in mice[43]. Notably, 174 of the 265 identified precursors (66%) contained both ductal and lobular morphology, suggesting that extension of precursors between dilated/nondilated pancreatic ducts and acinar lobules is a relatively common occurrence (Extended Data Fig 4d).

The role of fiber alignment in pancreatic cancer invasion

Next, we investigated the morphology of invasive pancreatic cancer and the tumor microenvironment in eight large samples. We first focused on the morphology of PDAC at the interface of invasive cancer and adjacent normal tissue in sample P7 to identify patterns of invasion, then enumerated the occurrence of these patterns in all tissues.

The mass consisted of a region of invasive carcinoma with three prominent protrusions extending into surrounding normal pancreatic tissue (Fig 6a). The first of these protrusions was invasive cancer extending within the lumen of a vein for at least 4mm. The second of the protrusions was a >3mm region of cancer extension along periductal stroma. The third protrusion was a >1mm focus of perineural invasion. We quantified the occurrence of these phenomena in all eight samples, revealing that all samples (100%) contained regions of venous invasion, seven (87%) contained perineural or neural invasion, and five (63%) contained invasion along periductal, perivascular, or perilobular stroma. As CODA allows confirmation of 3D findings in high-resolution H&E images, all foci of invasion were further validated via examination of the histology (Extended Data Figs 5, 6, 7).

Finally, we investigated 3D stromal properties at the pancreatic vasculature, ducts, and nerves. The alignment of collagen fibers in histological samples of PDAC has been negatively correlated with prognosis[44–46]. However, in previous work utilizing 2D samples of many patients, collagen alignment in the ductal submucosa of normal pancreatic ducts was reported to be low[45,47]. We sought to repeat this measurement to account for the angle of sectioning of the ducts.

Using our 3D renderings, we identified coordinates where the ducts, blood vessels, and nerves were cut at two extremes: perpendicular to the long axis of the structure (axially sectioned), and parallel to the long axis of the structure (longitudinally sectioned) and isolated these regions in H&E (Fig 6b) to quantify collagen fiber alignment. Our measurements of fiber alignment therefore account for the varying appearance of fibers

relative to their orientation to the sectioning blade, allowing more accurate calculation than can be computed from the random plane in a 2D histological section alone. As validation of our fiber alignment measure, we compare our results to measures of alignment of nerve fibers, which are known to be highly aligned in the longitudinal direction[48–50].

Quantification[51] revealed significantly higher (using the Wilcoxon rank sum test) collagen and nerve fiber alignment and nuclear aspect ratio in longitudinally compared to axially sectioned structures (Fig 6c). For nuclear aspect ratio, we measure a 2.1-, 2.3- and 2.5-fold change between longitudinally and axially sectioned images for periductal, perivascular, and perineural collagen, respectively (all p values $<10^{-5}$). For fiber alignment, we measure a 2.5-, 2.4-, 2.2-, and 2.2-fold change between longitudinally and axially sectioned images for periductal collagen, perivascular collagen, perineural collagen, and nerve fibers, respectively (all p values $<10^{-5}$). Contrary to previous works in 2D, these results suggest that collagen fibers are highly aligned along the longitudinal direction of structures they surround, including ducts, blood vessels, and nerves. This is the same direction of alignment as that of the observed cancer protrusions.

Discussion

Here we show that CODA is a powerful complement to tissue clearing and current serial sectioning techniques used to study 3D tissue microarchitecture. Tissue clearing is the most popular current approach to study 3D tissues, wherein intact samples are rendered semi-transparent, labeled, and imaged using confocal or light-sheet microscopy, and have been used to conduct landmark scientific research[13–18,52,53]. However, long wait times of days to weeks between protocol steps, inconsistent antibody penetration, limits on the size of tissues that can be cleared, the number of labels that can be used, and longstanding complications in quantification of the rendered 3D datasets represent key challenges in clearing research[21]. Current serial sectioning methods bypass some of the shortcomings of tissue clearing, albeit through introduction of new challenges. The sectioning of tissue causes unpredictable warping, requiring sophisticated registration techniques. Additionally, many serial sectioning methods rely on expensive techniques for labeling including IHC labeling, mass spectrometry, and manual annotation[23,24,33]. Though expensive, these 2D labels are easier to quantify than 3D data generated by clearing techniques, as they can take advantage of a plethora of previously developed 2D computational approaches[54–56].

CODA is a powerful tool that has potential to integrate many current tissue imaging techniques. It incorporates nonlinear image registration and deep learning techniques to create multi-labelled tissue volumes using H&E images, which is a relatively inexpensive histological technique. As our results demonstrate that CODA can derive quality 3D reconstructions while skipping at least two intervening sections, future addition of IHC labeling, spatial ‘omics’, and gene expression imaging to the intervening sections will increase the number of labels beyond what is currently achievable. The number of tissue and molecular phenotypes that CODA can label in the pancreas, skin, liver, and lungs has the potential to unlock previously unknown insights into human tissue, health, and disease.

In our analysis of pancreatic tumor progression, we identify several findings which are both novel and only possible through 3D analysis. We find that many anatomically separate precursor lesions can develop in small or large ducts, and that individual precursors commonly present both in the pancreatic ducts and in foci of ADM in the acinar lobules. We find invasive cancer cells extending from the central tumor along existing structures such as veins, nerves and peri- ductal, vascular, lobular, and neural collagen. Together with previous work which found highly aligned collagen to be a negative prognostic factor in PDAC[46], our identification of cancer cells protruding along aligned fibers suggests that pancreatic cancer cells *in-situ* may invade more easily in regions of aligned collagen and nerve fibers. Overall, there is a need in cancer research for 3D reconstruction techniques which enable the collection of large, quantifiable tissue datasets. We demonstrate that CODA is one such powerful technique.

Online Methods:

Data availability

Data is available upon request from the corresponding author.

Code availability

Code is available on the following GitHub page: https://github.com/ashleylk/CODA

Tissue acquisition and scanning

This retrospective study was approved by the Johns Hopkins School of Medicine institutional review board. Formalin-fixed, paraffin-embedded samples were sectioned every 4μm. Every third tissue section was stained using hematoxylin and eosin (H&E), with two sections every three held out. All tissues of sample P0 were scanned for validation that skipping two sections maintained registration and reconstruction accuracy. Tissues were scanned at x20 using a Hammamatsu Nanozoomer. These studies were approved by the Institutional Review Board of The Johns Hopkins Hospital.

Image registration

Cases contained series of tissue images scanned at 20x, corresponding to approximately 0.5μm/pixel. Openslide software was used to save reduced size copies of each image, corresponding to 8μm/pixel using nearest neighbor interpolation[1]. For each sample, the center image was identified as the point of reference ($image_n$), and global and elastic registration was calculated for all other images in the sample.

We performed registration on greyscale, Gaussian-filtered, down sampled (80μm/pixel resolution) versions of the high-resolution histological sections. Global registration transformations for a pair of preprocessed tissue images were found through iterative calculation of registration angle and translation via maximization of cross-correlation. Radon transforms of the images taken at discrete angles between 0 and 359 degrees were calculated. The maximum of the cross correlation of radon transforms of the images yielded registration angle, and the maximum of the cross correlation of the rotated tissue images yielded translation. Elastic registration was obtained by calculating rigid registration of

cropped image tiles at 1.5-mm intervals across the globally registered images at 8μm/pixel resolution. The resulting local, rigid registration fields were interpolated to the size of the 8μm/pixel resolution images. Finally, the registration fields were smoothed using a Gaussian filter with standard deviation of 2 pixels to produce a nonlinear, elastic registration transformation.

In order to account for images with large regions of tissue splitting or folding, rigid global registration was performed to sequentially register each $image_{n+/-m}$ to the three next closest images to center, $image_{n+/-(m+1)}$ $image_{n+/-(m+2)}$, and $image_{n+/-(m+3)}$. Quality of each of the three global registrations was assessed by comparing pixel-to-pixel correlation between the moving and each reference image. The registration with the best result was kept and the other two discarded. Thus, if $image_{n+/-(m+1)}$ contained large defects such as tissue splitting or folding, then $image_{n+/-(m+2)}$ would be used as the reference for rigid registration to avoid compound errors. Following global registration, elastic registration was employed between the moving image and chosen reference image to create a nonlinear displacement map. This process was repeated for all images in a sample such that all images were elastically registered to the coordinate system of the center $image_n$.

Assessment of image registration quality

Quality of image registration within the pancreas image datasets was calculated using pixel-wise Spearman correlation. ‘True’ biological pixel variation was calculated by correlating pixel intensity along the x and y dimensions of single images (longitudinal correlation). It was assumed that ‘perfect’ registration would result in a similar z-direction (down the image stack) correlation to the xy correlation, as the xy correlation represents the variation in pixel intensity in intact tissue. Axial pixel correlation was calculated by correlating pixel intensity along the z dimension of serial images. Unregistered z-correlation was compared to post-global registration correlation and post-elastic registration correlation to determine improvements to intensity continuity following registration, and post-elastic registration was compared to longitudinal correlation to determine how closely our registration results could emulate the true intensity variation between connected tissue.

For each correlation calculation (along the xy direction, unregistered z-dimension, global registered z-dimension, and elastic registered z-dimension) Spearman correlation was calculated for pixels at 4μm intervals starting at 0 micron apart. Correlation of pixels 0 micron apart is correlation of each pixel to itself (equal to 1). Correlation of pixels 4μm corresponds to two pixels 4μm apart in a single image (for the xy calculation) or one image apart (for the z calculation). This process was repeated for distances up to 0.3 mm. Additionally, this process was repeated for registration of all images in sample P0, and registration of one in two, one in three, one in four, and one in five images in P0 to prove that we maintain >95% correlation when sampling one in every three images per tissue sample.

Comparison of image registration to existing techniques

CODA registration was applied to a publicly available serial histological sample of 260 mouse prostate images, which was part of a previously published paper comparing

the performance of seven registration techniques.[2] The image dataset contained manual annotation of two cells per image each from two different researchers. Performance metrics included pairwise target registration error (TRE): average distance between pairs of fiducial markers; accumulated target registration error (ATRE): estimation of accumulated distortion throughout the stack; root mean squared error (RMSE): pairwise comparison of pixel intensities across the stack; Jaccard Index (J): pairwise area overlap of consecutive images; and (dA): change in area of the tissue slides pre- and post- registration. CODA performed similarly to competing techniques in TRE, J, and dA. Importantly, CODA outperformed all other techniques in ATRE and RMSE, suggesting CODA registration of this sample resulted in less accumulated error than other techniques.

Raw performance metrics are listed in the source data file for figure 2A. As the magnitude of various performance metrics varied widely, normalized performance metrics were calculated such that a single graph could concisely express a wide variety of performance parameters. Mean performance metrics were normalized using the following formulas such that they lay within the range of 0 – 1 and such that higher numbers indicate better performance:

$$TRE_{Normalized} = 1 - TRE_{mean}/\max(TRE_{mean})$$

$$ATRE_{Normalized} = 1 - ATRE_{mean}/\max(ATRE_{mean})$$

$$RMSE_{Normalized} = 1 - RMSE_{mean}/\max(RMSE_{mean})$$

$$RMSE_{Normalized} = 1 - RMSE_{mean}/\max(RMSE_{mean})$$

$$J_{normalized} = J_{mean}/\min(J_{mean}) - 1$$

$$dA_{Normalized} = 1 - |dA_{mean}|/\max(|dA_{mean}|) \quad [\text{where } |x| \text{denotes absolute value of x}]$$

Identification of cells in histological samples

First, the hematoxylin channel of all H&E images was extracted using color deconvolution. Openslide software was used to save reduced size copies of all tissue images, corresponding to 2μm/pixel using nearest neighbor interpolation. For each image, the tissue region of the image was identified by finding regions of the image with low green channel intensity and high red-green-blue (rgb) standard deviation. Next, rgb channels were converted to optical density. Using kmeans clustering analysis, 100 clusters were identified to represent the optical densities of the image. The most common, blue-favored optical density was chosen to represent the hematoxylin channel, and the most common, red-favored optical density was chosen to represent the eosin channel. The background optical density was fixed as the

inverse of the average of the hematoxylin and eosin optical densities. These three optical densities were used to deconvolve the rgb image into hematoxylin, eosin, and background channel images. Using methods described in ref[3], the hematoxylin channel images were smoothed, and 2D intensity minima of a designated size and distance from each other were identified as nuclei.

Validation of cell detection algorithm and comparison to existing techniques

A total of five 1.5mm^2 regions were randomly extracted from the serial images for validation. For each region, two researchers manually annotated cells using an annotation function built in MATLAB 2021b. Next, CODA cell detection and two popular cell detection algorithms (Hovernet and QuPath)[4,5] were applied to the validation images to automatically generate nuclear coordinates. Automatically generated coordinates were termed true positives if they were within 2μm of a manually generated coordinate (that was not already paired with another automatically generated coordinate). 2μm was selected as the radius as this was determined to be the average radius of nuclei in the images. Automatically generated coordinates were termed false positives if they were not within 2μm of a manually generated coordinate (that was not already paired with another automatically generated coordinate). Finally, manually annotated coordinates with no corresponding automatically generated coordinate were termed false negatives. From the true positives, false positives, and false negatives, precision and recall were calculated to compare each of the three techniques to both sets of manual annotations.

Deep learning tissue multi-labelling

A deep learning model was created for each case using manual tissue annotations of that sample. Openslide software was used to save reduced size copies of all tissue images, corresponding to 2μm/pixel using nearest neighbor interpolation[1]. Seven tissue images equally spaced within each sample were extracted. For each of the seven images, we manually annotated 50 examples of each identified tissue subtype using Aperio ImageScope, creating .xml files of annotation coordinates. Annotation coordinates were loaded into MATLAB 2021b using publicly available software and were downsampled to correctly overlay on the 2μm/pixel tissue images[6].

In order to reduce the heterogeneity of the H&E images, the H&E stain of all tissue images in each case were normalized. Using the hematoxylin and eosin channel images created for the cell counting analysis and the optical density calculated for a reference H&E image from the same case, we reconstructed rgb images of each tissue type to a chosen optical density. Incorporation of image color normalization allowed us to avoid catastrophic failure of the semantic segmentation on unannotated images with drastically different staining patterns.

Bounding boxes of all annotations were identified and each annotated rgb image region was extracted and saved as a separate image file. A matrix was used to keep track of which bounding box images contained which annotation tissue types. Training images were built through creation of a 9000 × 9000 × 3, zero-value rgb image tile. Annotation bounding boxes containing the least represented deep learning class were randomly overlaid on the blank image tile until the tile was >65% full of annotations and such that the number of

pixels of each deep learning class was approximately equal. Annotation bounding boxes were randomly augmented via rotation, scaling by a random factor between 0.8–1.2, and hue augmentation by a factor of 0.8–1.2 in each rgb color channel. The 9000 × 9000 × 3 image tile was then cut into 324 500 × 500 × 3 images. 20 such large images were built, half with augmentation, to create 6480 training images, and 5 additional images were built to create 1620 validation images. 324 testing images were created using manual annotations from an image not used for training or validation. This data generation pipeline including the size of the image tile, size of the training tiles, and levels of data augmentation was chosen as it gave highest performance during pilot classification of sample P0.

Following dataset creation, a resnet50 network was adapted for DeepLab v3+ semantic segmentation[35] and trained to a validation patience of 5. If 90% tissue subtype precision and recall was not obtained, additional manual annotations were added to the training and testing images and the process was repeated until desired accuracy was reached. We determined that >90% precision and recall resulted in classified models that generally matched pathological annotation of diseased tissues. Once a satisfactory deep learning model was trained, all tissue images in the sample were semantically segmented to create labelled tissue images with a pixel resolution of 2μm/pixel.

Addition of nerve labels to previously deep learning-labelled tissue images

The model design explained above was utilized to add nerves to the previously labelled pancreas histological images. First, 50 nerve annotations per image were collected on the images used for training of the previous deep learning model. Next, collagen, blood vessel, and whitespace annotations from all previous annotation datasets were pooled. All other tissue components (islets, normal ductal epithelium, acini, precancers, cancer, and lymph node) were pooled to a fifth class termed ‘other tissue’. Collagen and blood vessel annotations were kept as separate classes as the eosin-rich staining on these structures closely resembles the staining pattern on nerves. It was found through training of a tri-class model (nerves, whitespace, other tissue only) that nerves would often be confused with collagen and vascular structures. The five annotation classes were pooled into training tiles as is described above and a semantic segmentation network with >90% precision and recall per class was trained across all thirteen pancreas samples. It was calculated that >97% of pixels replaced by the nerve label were previously classified (using the semantic segmentation network that did not contain nerves as a label) as either collagen or vasculature. As this network classified both nerves and ‘other tissue components’, the nerve classification in this trained model was assumed to supersede the previous classification (thus all pixels labelled as nerves replaced the label for that pixel generated by the previous, 10-class model).

3D reconstruction of samples

Multi-labelled images created by the deep learning portion of the CODA pipeline were consolidated into a 3D matrix using the H&E image registration results. Similarly, cellular coordinates counted on the unregistered histological sections were consolidated into a 3D cell matrix using the H&E image registration results. 3D renderings of the labelled tissue regions were visualized using the “patch” and “isosurface” commands in MATLAB 2021b

and using a color scheme with a unique rgb triplet for each tissue subtype. Dimensions of rendered tissues were calculated in xy using the pixel resolution of the original x20 scanned histological sections (approximately 0.5μm/pixel) and using the tissue section spacing (4μm) in z. The resolution of the 3D renderings was 2μm/pixel in xy, the resolution used for image semantic segmentation, and 12μm/pixel in z, as only one in three tissue sections were used in the analysis. Single cells were visualized within the 3D renderings using the "scatter3" command in MATLAB 2021b. For all calculations performed on the 3D labelled matrices of the tissues, the 3D matrix was subsampled using nearest neighbor interpolation from original voxel dimensions of $2 \times 2 \times 12\mu m^3$/voxel to an isotropic $12 \times 12 \times 12\mu m^3$/voxel.

Calculation of tissue content, bulk cell density, and local cell density

Tissue composition was calculated by counting the total number of voxels in the isotropic 3D matrix corresponding to each tissue subtype and dividing those numbers by the total number of voxels in the tissue region of the 3D matrix. These tissue compositions were formatted into a matrix in MATLAB 2021b and visualized as a heatmap.

Cell density of each tissue subtype was calculated by combining the tissue subtype data in the multi labelled 3D matrix with cell coordinate data in the cell 3D matrix. Cells at each voxel in the cell 3D matrix corresponded to the tissue subtype label in the multi labelled 3D matrix (for example, a cell is labelled an epithelial cell if the nuclear coordinate was identified in a region labelled as epithelium by the deep learning pipeline). Measurements of nuclear diameter were used to estimate true 3D cell counts from the 2D cell coordinates. Using Aperio ImageScope, 100 nuclei of each tissue subtype were measured for each case. The estimated 3D cell count (C_{3D}) of cells 715 counted on serial sections analyzed every three sections was calculated using the formula:

$$C_{3D} = \sum_{images} \sum_{subtypes} C_{image} \frac{3T}{T + D_{subtype}}$$

where C_{image} is the cell count for a given tissue image, T is the thickness of the histological section, and $D_{subtype}$ is the measured diameter of a nucleus for a tissue subtype. For each tissue subtype, bulk 3D cell density was calculated by dividing the 3D extrapolated cell count of a particular subtype divided by the total volume of the tissue. Local 3D cell density was calculated by dividing the 3D extrapolated cell count of a particular subtype divided by the volume of that particular tissue subtype.

Determination of spatially distinct precursor lesions

The 3D multi labelled matrices were used to determine tissue connectivity. Following classification, all objects labelled as pancreatic precancers lesions were visually verified to be precancers through creation of bounding box serial sections. Independent precursors were identified in the 3D multi labelled matrix using the "bwlabeln" command in MATLAB 2021b. "Bwlabeln" identifies and labels spatially distinct objects in matrices. We calculated connectivity on both the precancers alone and the precancers plus the normal ductal epithelium. Distinct precancers and cancers identified using "bwlabeln" could then be quantitatively analyzed or 3D rendered independently from other precancers.

Independent precursor coordinates were used to automatically annotate connected lesions on H&E images of 2μm/pixel resolution. First, each precursor was assigned a distinct RGB color. Next, for each registered H&E image in the serial sections, the number of distinct precursors appearing on that section was determined. For each independent precursor on the section, voxels defining the precursor in the volume matrix were located. The pixels were dilated and only the outline kept, then rescaled to match the 2μm/pixel H&E images such that the annotated precursor mask was reformatted to appear as a thick outline overlayed on the precursor region of the H&E section. The outline was overlayed on H&E and the pixels in the H&E image corresponding to the outline were recolored to match the color defining that independent precancer. This was repeated for all precancers in the sample. The same coloring scheme for each precancer was then used in a 3D reconstruction of the sample, allowing users to match precancer histology to the correct 3D reconstructed precancer.

To create the graph in Fig. 5B, the number of precursors present in each sample was calculated. First, we determined the number of lesions present on each 2D section (not considering 3D connectivity). Next, we determined the true number of precursors present on each section when considering 3D connectivity. For each section in which at least one precursor was present, the number of (distinct in 2D space) precursor-classified objects was normalized by the number of (distinct in 3D space) precursor-classified objects that were present on the section. The average and standard deviation of this ratio for each sample was calculated and plotted.

Finally, metrics were performed on each independent precancer to determine 3D morphology. Using the 3D reconstructions and serial bounding boxes of each precancer, we determined 3D phenotype by assessing 3D presentation as well as the location of the precancer in the pancreatic ducts or pancreatic acinar lobules. Next, cell count was determined by counting the number of cells located in the same voxel coordinates as each defined precursor lesions and corrected using the 3D cell conversion equation listed above. Precursor volume was calculated by summing the number of voxels defining each precancer and converting from voxel to mm^3 units (1 voxel = $12*12*12*10^{-9}$ mm^3). Precursor cell density was calculated by dividing cell number per precursor by precursor volume. Precursor primary axis length was determined using the function “regionprops3” in MATLAB2021b.

Calculation of collagen and nerve fiber alignment and nuclear aspect ratio

Using the 3D renderings, we identified three coordinates of axial sectioning and three coordinates of longitudinal sectioning around pancreatic ductal epithelium, blood vessels, and nerves for seven samples containing large regions of normal pancreatic parenchyma (for 42 total images of ducts, nerves, and blood vessels each). We located the 2D histological sections using 3D coordinates of the identified regions and cropped the region of interest from the corresponding x20 H&E images. We applied the color deconvolution method described above to the cropped 20x H&E image to separate the hematoxylin and eosin channels. We calculated fiber alignment within selected 2500 μm^2 windows in the eosin channel images using a previously developed method[7]. By measuring fiber alignment within collagen or nerve regions in images of axial or longitudinal sectioning, we can compare the degree of collagen and nerve fiber alignment in axially and longitudinally sectioned regions

of the ducts, blood vessels, and nerves. An alignment index of one represents completely aligned matrix of fibers and an alignment index of zero represents an isotropic matrix of fibers. We measured the alignment index at two locations of each cropped image.

We next manually measured nuclear aspect ratio of cells within the peri-ductal/vascular/neural space using a script written in MATLAB 2021b. To confirm the accuracy of the measurements, two scientists measured five randomly selected cells in each image, for a total of 1260 cells measured. The nuclear aspect ratio measurements between the two researchers were compared in Extended Data Fig. 4E and the differences were shown to be statistically insignificant. Violin plots were constructed from data using code available in the provided reference[8].

Construction of z-projections

The 3D labelled matrices of each sample were used to construct z-projections of each tissue subtype. For each subtype, the pixels of the 3D matrix corresponding to that subtype were summed in the z-dimension, creating a projection of the volume on a plane perpendicular to the xy axes. The projections were normalized by their maximum and visualized using the imagesc command in MATLAB 2021b using the same color scheme created for visualization of the 3D tissues.

Analysis of normal and atrophic pancreatic lobules

For sample P7, the 3D model revealed a large region of acinar atrophy. Using an annotation pipeline written in MATLAB 2021b, registered, serial H&E images were rapidly displayed and manually annotated. In each image, the boundaries of the atrophic lobule and a nearby normal lobule were segmented. These regions were 3D reconstructed and tissue compositions were calculated using the methods described above.

Confusion Matrices

Quality of the deep learning models was visualized using construction of confusion matrices. For each datapoint in the testing dataset, the ‘true’ label (as manually annotated in H&E) was determined and matched with the ‘determined’ label (as classified by the deep learning model. A table was constructed to display the number of datapoints corresponding to each true label and their corresponding determined labels, as well as per-class precision and recall and overall model accuracy.

Statistics & Reproducibility

No statistical method was used to predetermine sample size. No data were excluded from the analyses. All statistical analyses were performed using the Wilcoxon rank sum test. All results may be duplicated from the available source data files or the 3D datasets.

Extended Data

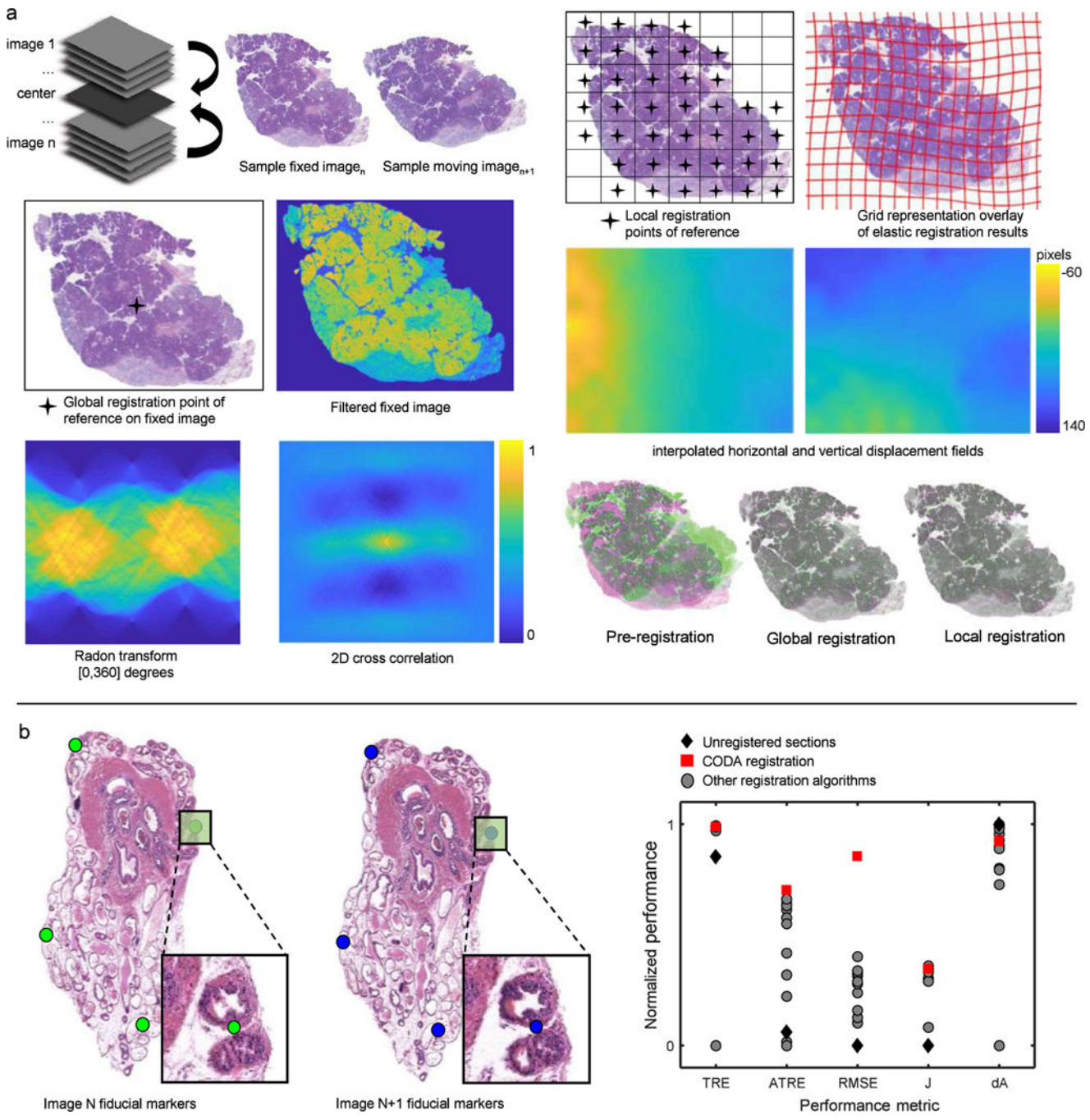

Extended Data Fig 1. Histological image registration sample workflow.

(a) Tissue cases registered with reference at center z-height of sample. Example fixed and moving images shown. Global registration performed with rotational reference at center of fixed image. Fixed and moving images smoothed by conversion to greyscale, removal of non-tissue objects in image, intensity complementing, and Gaussian filtering to reduce pixel-level noise in images. Radon transforms calculated filtered fixed and moving for

discrete degrees 0–360. Maximum of 2D cross correlation of radon transforms yields registration angle. Maximum of 2D cross correlation of filtered images yields registration translation. Local registration performed at discrete intervals across fixed image. For each reference point, tiles are cropped from fixed and moving images and coarse registration is performed on tiles. Results from all tiles are interpolated on 2D grids to create nonlinear whole-image displacement fields. Sample overlays of pre and post registration. **(b)** Sample validation image from ref[33] . with overlayed fiducial points. Normalized performance metrics (explained in further detail in supplementary materials).

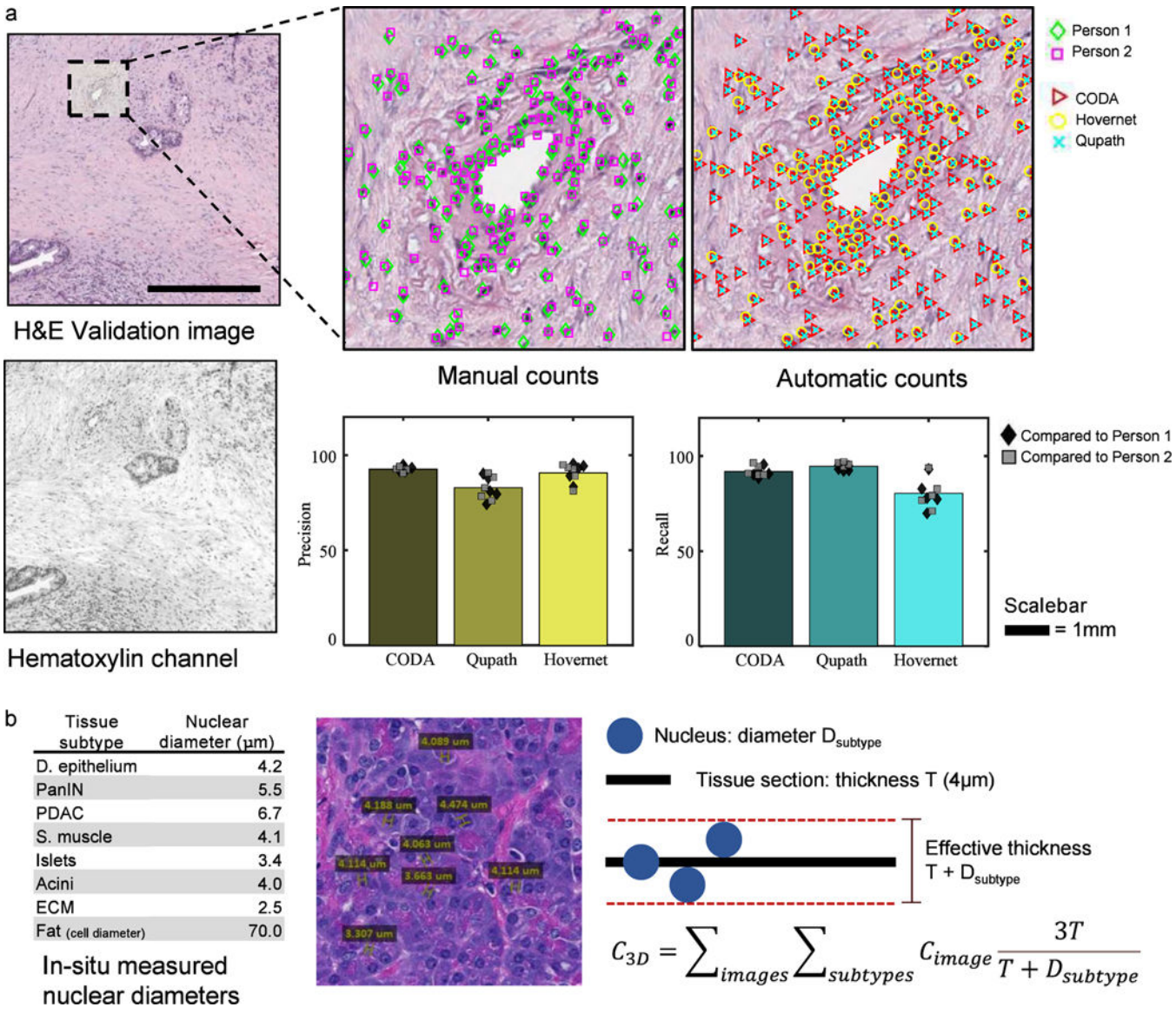

Extended Data Fig 2. Validation of cell count and 2D to 3D cell count extrapolation.

(a) Sample histological section and corresponding color deconvolved hematoxylin channel of image. All cells in five validation images were manually annotated by two persons. Annotations were compared to CODA outputs and outputs from two existing cell counting methods[27,28]. **(b)** Cell diameters of each tissue subtype were measured using Aperio

ImageScope. 2D cell counts were extrapolated to 3D using the formula listed. It was assumed that cells could be detected by the algorithm if any part of the nucleus touched the tissue section. Therefore, effective tissue section thickness equals true tissue section thickness plus the diameter of the cell. 3D cell counts were estimated by multiplying 2D cell counts by the true thickness of the tissue section, multiplied by three because two sections were skipped during scanning, divided by the effective thickness of the section.

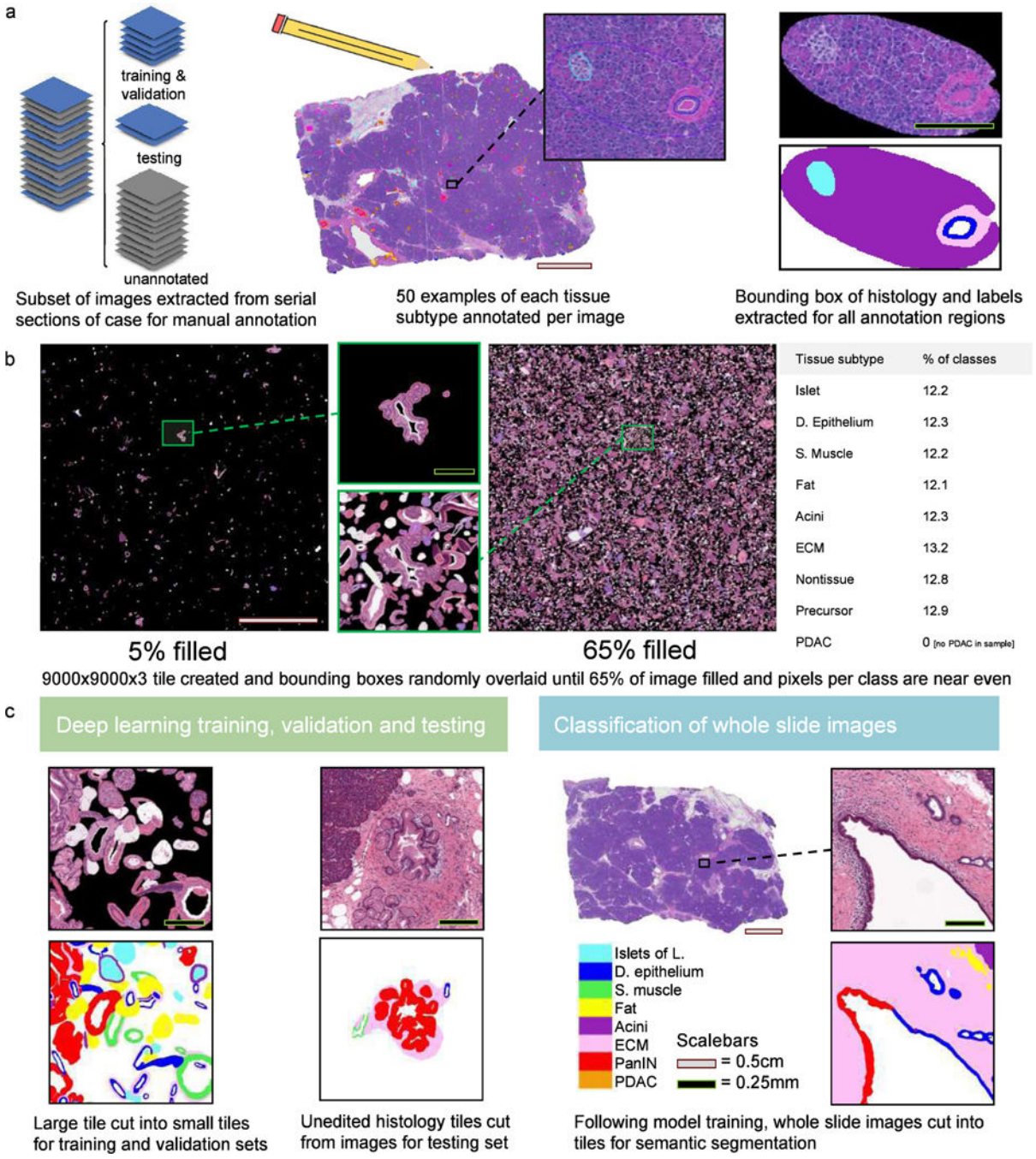

Extended Data Fig 3. Overview of semantic segmentation workflow and training data design.

(a) For each case, a minimum of seven images were extracted from for manual annotation. For each extracted image, minimum 50 examples of each tissue type were annotated, and the annotations cropped from the larger image. **(b)** To construct training and validation sets, cropped annotations were overlayed on a large image until the image was >65% full and such that the number of annotations of each type was roughly equal. **(c)** These large tiles were cut into smaller tiles for training and validation. Additional tiles were created for the testing set where the annotation was not cropped from the image. Testing accuracy was assessed as the percentage of the annotated area of the tile classified correctly. Following model training, the serial images were cropped into tiles and semantically segmented.

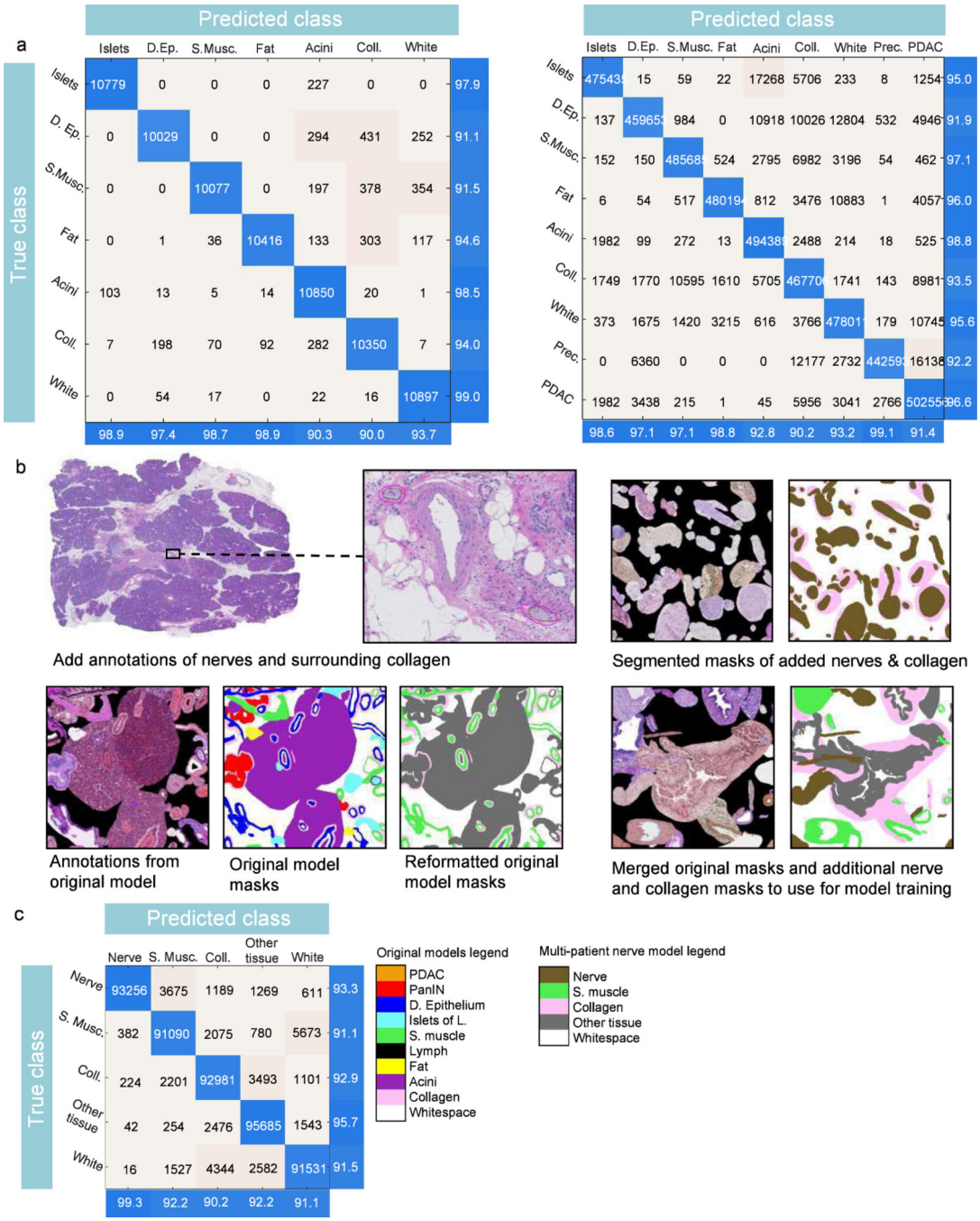

Extended Data Fig 4. Sample deep learning accuracy and multi-patient model.

(a) Sample predicted vs. true outcomes for deep learning models for sample PI (left) and P8 (right). **(b)** Workflow for creation of multi-patient semantic segmentation of nerves. Nerve annotations collected from thirteen pancreas samples. Original tissue annotations reformatted to: l . smooth muscle, 2. collagen, 3. other tissue (islets, normal ducts, acini, precursor, lymph, PDAC), 4. white (whitespace, fat). Nerve annotations combined with original annotations to create a dataset for nerve recognition in H&E images. **(c)** Predicted vs. true outcomes for multi-patient nerve detection model.

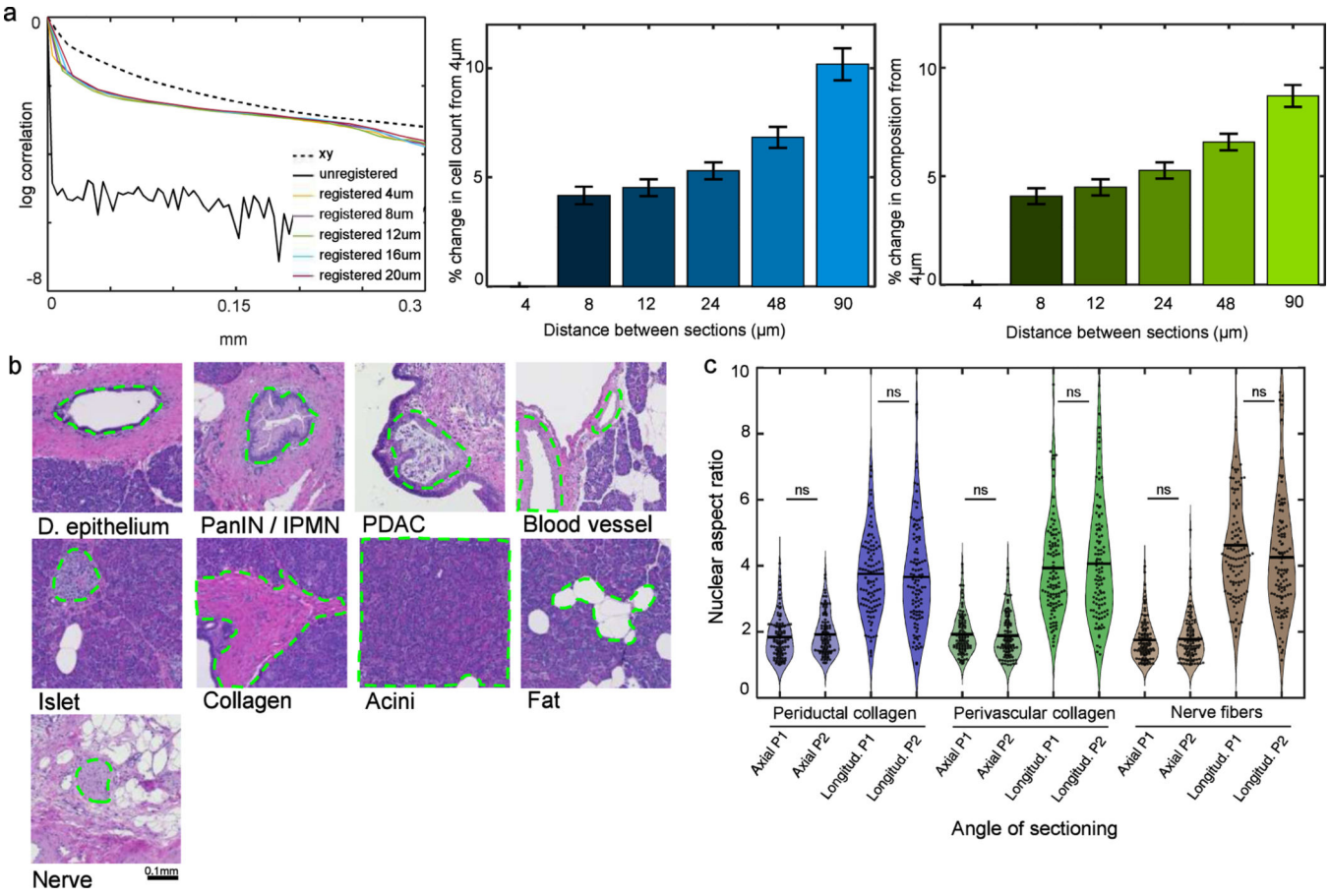

Extended Data Fig 5. Additional methodological supplemental.

(a) Quantification of loss in quality due to reducing the z-resolution of serial samples. Calculation of pixel correlation across the z-axis (Left) shows that >95% correlation is maintained post-registration when skipping up to four serial sections, or 20µm, between each H&E collected. Calculation of % change in cell count (center) and tissue composition (right) reveals <5% error in 3D cell count and tissue composition extrapolation when skipping up to two serial sections, or 12µm, between each H&E collected). **(b)** Tissues labelled by CODA in H&E-stained tissue sections of human pancreas. **(c)** Comparison of nuclear aspect ratio measurements performed by person I and person 2 show nonsignificant differences between measurements.

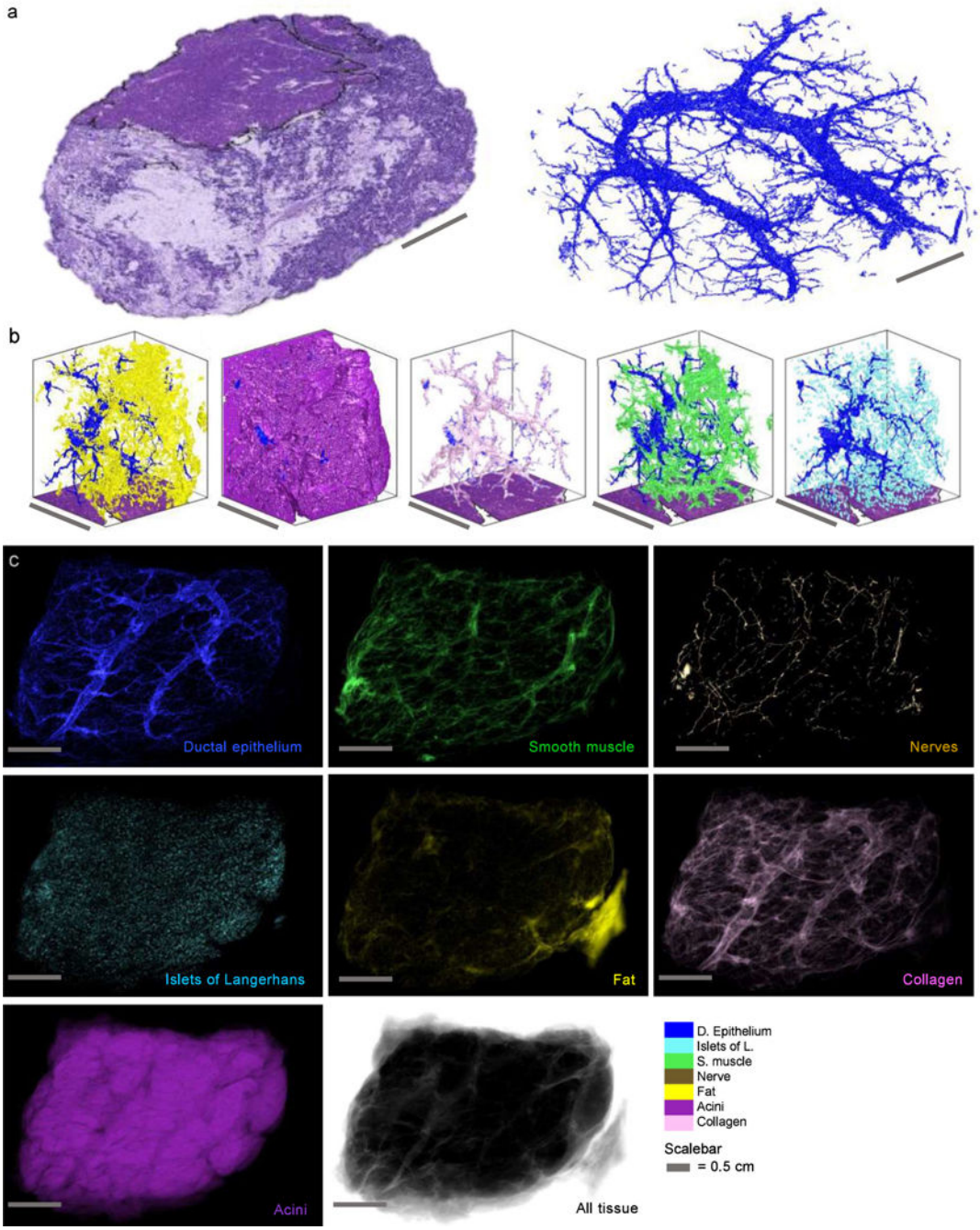

Extended Data Fig 6. 3D reconstruction of sample P1.

(a) Global reconstruction of and ducts. **(b)** 3D rendering of subregions, showing ducts, fat, acini, collagen, blood vessels, and islets of Langerhans. **(c)** Z-projections of labelled tissues (intensities enhanced for visibility).

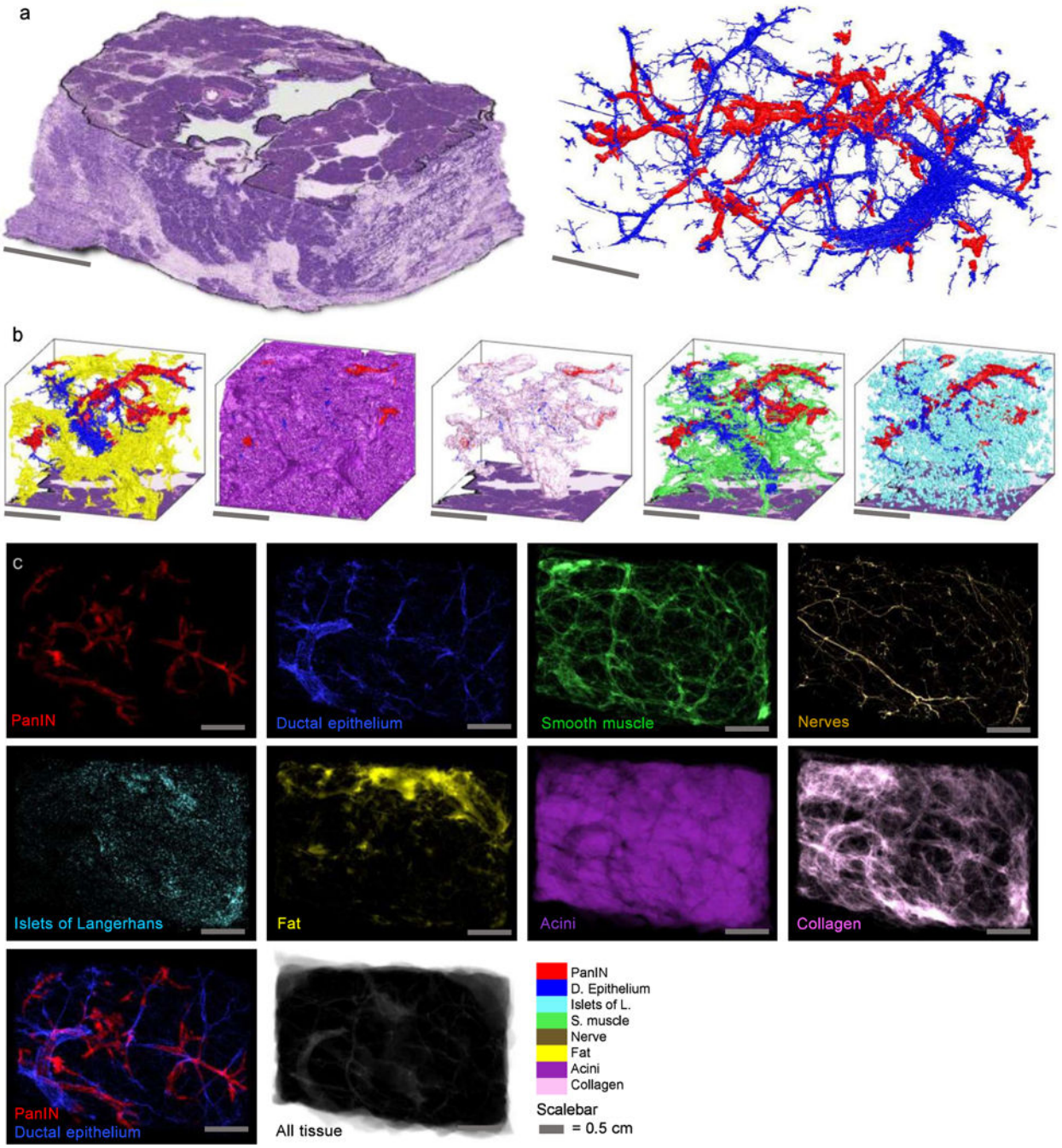

Extended Data Fig 7. 3D reconstruction of sample P2.

(a) Global reconstruction of H&E, ducts, and PanIN. **(b)** 3D rendering of subregions, showing PanIN, ducts, fat, acini, collagen, blood vessels, and islets of Langerhans. **(c)** Z-projections of labelled tissues (intensities enhanced for visibility).

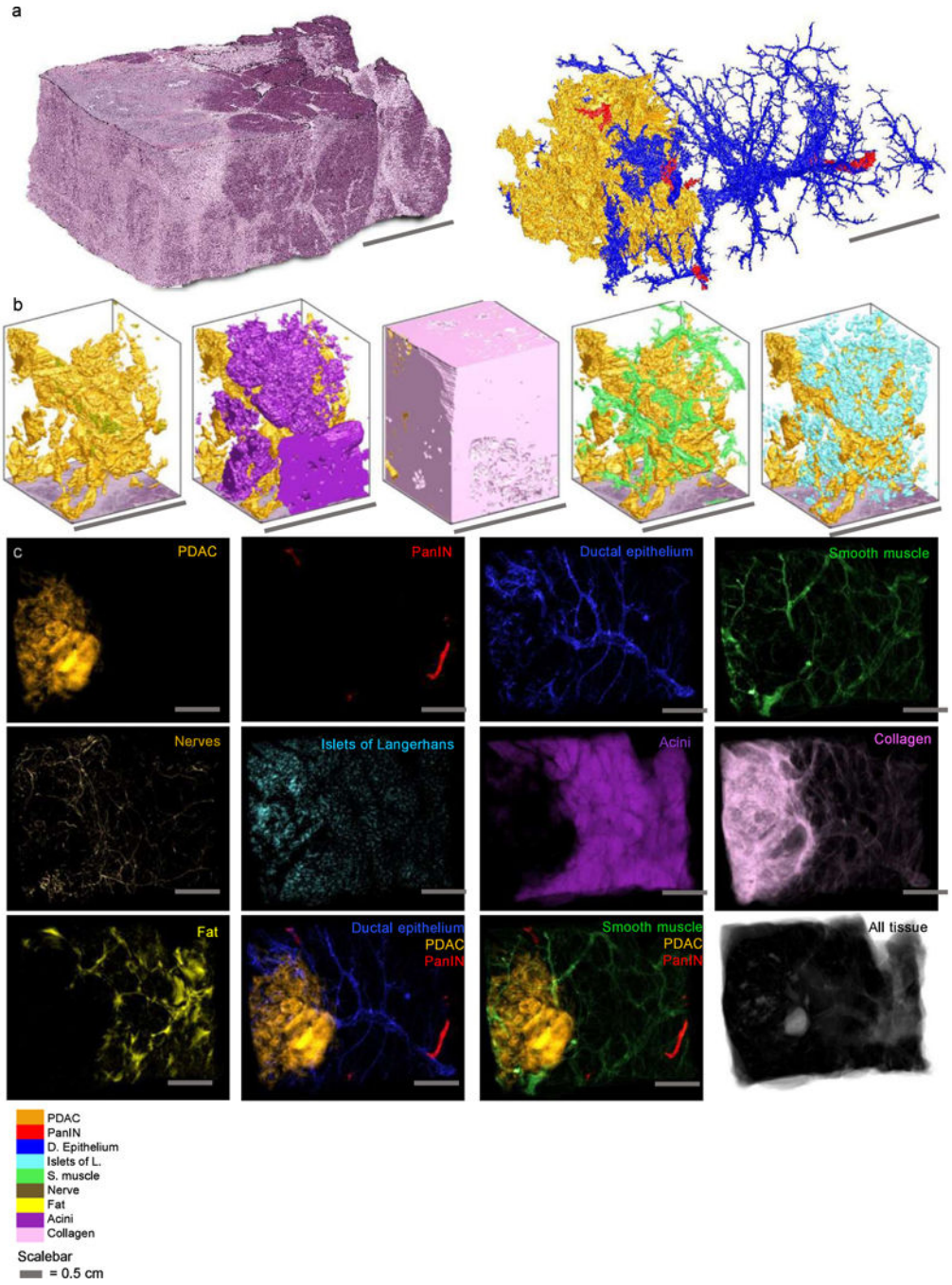

Extended Data Fig 8. 3D reconstruction of S05-PDAC.

(a) Global reconstruction of H&E, ducts, PanIN, and PDAC. **(b)** 3D rendering of subregions, showing PDAC, PanIN, ducts, fat, acini, collagen, blood vessels, and islets of Langerhans. **(c)** Z-projections of labelled tissues (intensities enhanced for visibility).

Supplementary Material

Refer to Web version on PubMed Central for supplementary material.

Acknowledgements:

We would like to thank Prof Jude Phillip and Prof. Danielle Gilkes for their important feedback in this work. We would additionally like to thank sources of funding for additional projects in our groups: NIH/NCI P50 CA62924; NIH/NIDDK K08 DK107781; Sol Goldman Pancreatic Cancer Research Center; Buffone Family Gastrointestinal Cancer Research Fund; Carol S. and Robert M. Long Pancreatic Cancer Research Fund; Allegheny Health Network-Johns Hopkins Cancer Research Fund; American Cancer Society - The Cornelia T. Bailey Foundation Research Scholar Grant RSG-18-143-01; AACR-Bristol-Myers Squibb Midcareer Female Investigator Grant; Emerson Collective Cancer Research Fund; Robert L. Fine Pancreatic Cancer Research Foundation; Rolfe Pancreatic Cancer Foundation; Joseph C Monastra Foundation; The Gerald O Mann Charitable Foundation (Harriet and Allan Wulfstat, Trustees); Susan Wojcicki and Denis Troper; The Carl and Carol Nale Fund for Pancreatic Cancer Research. The Johns Hopkins University Oncology Tissue Services core used for sectioning and staining is funded by the SKCCC Cancer Center Support Grant (CCSG; P30 CA006973)

Funding:

National Institutes of Health / National Cancer Institute U54CA268083. (DW, PW, ALK)

National Institutes of Health / National Cancer Institute U52CA210173. (DW)

National Institutes of Health / National Institute on Aging U01AG060903. (DW)

The Sol Goldman Pancreatic Cancer Research Center. (AMB, LDW, FA, EDT, RHH, PW, DW)

Susan Wojcicki and Dennis Troper. (AMB, LDW, FA, EDT)

The Rolfe Foundation for Pancreatic Cancer Research, Allegheny Health Network – Johns Hopkins Cancer Research Fund. (AMB)

ARCS Foundation, Inc. (ALK)

Nanotechnology for Cancer Research T32 Training Grant 5T32CA153952. (ALK)

NVIDIA GPU Grant. (DW)

References:

1. Liebig C, Ayala G, Wilks JA, Berger DH & Albo D. Perineural invasion in cancer. Cancer 115, 3379–3391 (2009). [PubMed: 19484787]
2. Hong SM et al. Three-dimensional visualization of cleared human pancreas cancer reveals that sustained epithelial-to-mesenchymal transition is not required for venous invasion. Mod. Pathol. 2019 334 33, 639–647 (2019).
3. Siegel RL, Miller KD, Fuchs HE & Jemal A. Cancer Statistics, 2021. CA. Cancer J. Clin. 71, 7–33 (2021). [PubMed: 33433946]
4. Michaud DS et al. Physical Activity, Obesity, Height, and the Risk of Pancreatic Cancer. JAMA 286, 921–929 (2001). [PubMed: 11509056]
5. Hruban RH et al. Why is pancreatic cancer so deadly? The pathologist's view. J. Pathol. 248, 131–141 (2019). [PubMed: 30838636]
6. Tanaka M. et al. Meta-analysis of recurrence pattern after resection for pancreatic cancer. Br. J. Surg. 106, 1590–1601 (2019). [PubMed: 31454073]
7. Zhang J-FR Y.-W. W. Y. -M D -JJ Influence of Perineural Invasion on Survival and Recurrence in Patients with Resected Pancreatic Cancer. Asian Pacific J. Cancer Prev. 14, 5133–5139 (2013).
8. Huang L. et al. Ductal pancreatic cancer modeling and drug screening using human pluripotent stem cell– and patient-derived tumor organoids. Nat. Med. 2015 2111 21, 1364–1371 (2015).
9. Drost J. & Clevers H. Organoids in cancer research. Nat. Rev. Cancer 2018 187 18, 407–418 (2018).
10. Taniuchi K. et al. Overexpressed P-Cadherin/CDH3 Promotes Motility of Pancreatic Cancer Cells by Interacting with p120ctn and Activating Rho-Family GTPases. Cancer Res. 65, 3092–3099 (2005). [PubMed: 15833838]

11. Plentz R. et al. Inhibition of γ-Secretase Activity Inhibits Tumor Progression in a Mouse Model of Pancreatic Ductal Adenocarcinoma. Gastroenterology 136, 1741–1749.e6 (2009). [PubMed: 19208345]
12. Cruz-Monserrate Z. et al. Detection of pancreatic cancer tumours and precursor lesions by cathepsin E activity in mouse models. Gut 61, 1315–1322 (2012). [PubMed: 22068166]
13. Yang B. et al. Single-Cell Phenotyping within Transparent Intact Tissue through Whole-Body Clearing. Cell 158, 945–958 (2014). [PubMed: 25088144]
14. Murakami TC et al. A three-dimensional single-cell-resolution whole-brain atlas using CUBIC-X expansion microscopy and tissue clearing. Nat. Neurosci. 2018 214 21, 625–637 (2018).
15. Susaki EA et al. Versatile whole-organ/body staining and imaging based on electrolyte-gel properties of biological tissues. Nat. Commun. 2020 111 11, 1–22 (2020).
16. Zhao S. et al. Cellular and Molecular Probing of Intact Human Organs. Cell 180, 796–812.e19 (2020).
17. Chung K. et al. Structural and molecular interrogation of intact biological systems. Nat. 2013 4977449 497, 332–337 (2013).
18. Richardson DS & Lichtman JW Clarifying Tissue Clearing. Cell 162, 246–257 (2015). [PubMed: 26186186]
19. Xie W. et al. Prostate Cancer Risk Stratification via Nondestructive 3D Pathology with Deep Learning–Assisted Gland AnalysisProstate Cancer Risk Stratification via 3D Gland Analysis. Cancer Res. 82, 334–345 (2022). [PubMed: 34853071]
20. Hahn M. et al. Mesoscopic 3D imaging of pancreatic cancer and Langerhans islets based on tissue autofluorescence. Sci. Reports 2020 101 10, 1–11 (2020).
21. Liu JTC et al. Harnessing non-destructive 3D pathology. Nat. Biomed. Eng. 2021 53 5, 203–218 (2021).
22. Groot A. E. de et al. Characterization of tumor-associated macrophages in prostate cancer transgenic mouse models. Prostate 81, 629–647 (2021). [PubMed: 33949714]
23. Song Y, Treanor D, Bulpitt AJ & Magee DR 3D reconstruction of multiple stained histology images. J. Pathol. Inform. 4, 7 (2013). [PubMed: 23869286]
24. Lotz JM et al. Integration of 3D multimodal imaging data of a head and neck cancer and advanced feature recognition. Biochim. Biophys. Acta - Proteins Proteomics 1865, 946–956 (2017). [PubMed: 27594533]
25. Lotz N. et al. Zooming in: high resolution 3D reconstruction of differently stained histological whole slide images. 10.1117/12.2043381 9041, 16–22 (2014).
26. Tempest N. et al. Histological 3D reconstruction and in vivo lineage tracing of the human endometrium. J. Pathol. 251, 440–451 (2020). [PubMed: 32476144]
27. Rees J. et al. O36 Investigating clonal expansions in the normal stomach and the 3D architecture of oxyntic gastric glands. Gut 70, A20–A21 (2021).
28. Graham S. et al. Hover-Net: Simultaneous segmentation and classification of nuclei in multi-tissue histology images. Med. Image Anal. 58, 101563 (2019).
29. Bankhead P. et al. QuPath: Open source software for digital pathology image analysis. Sci. Reports 2017 71 7, 1–7 (2017).
30. Chan L. et al. HistoSegNet: Semantic Segmentation of Histological Tissue Type in Whole Slide Images. 10662–10671 (2019).
31. Ternes L. et al. VISTA: VIsual Semantic Tissue Analysis for pancreatic disease quantification in murine cohorts. Sci. Reports 2020 101 10, 1–12 (2020).
32. Magee D. et al. Histopathology in 3D: From three-dimensional reconstruction to multi-stain and multi-modal analysis. J. Pathol. Inform. 6, 6 (2015). [PubMed: 25774317]
33. Roberts N. et al. Toward Routine Use of 3D Histopathology as a Research Tool. Am. J. Pathol. 180, 1835–1842 (2012). [PubMed: 22490922]
34. Kartasalo K. et al. Comparative analysis of tissue reconstruction algorithms for 3D histology. Bioinformatics 34, 3013 (2018). [PubMed: 29684099]
35. Wu PH et al. High-throughput ballistic injection nanorheology to measure cell mechanics. Nat. Protoc. 2012 71 7, 155–170 (2012).

36. Chen L-CZ, Yukun; Papandreou, George; Schroff, Florian; Adam, H. Encoder-Decoder with Atrous Separable Convolution for Semantic Image Segmentation. Proc. Eur. Conf. Comput. Vis. 801–818 (2018).
37. Basturk O. Et Al. A Revised Classification System And Recommendations From The Baltimore Consensus Meeting For Neoplastic Precursor Lesions In The Pancreas. Am. J. Surg. Pathol. 39, 1730 (2015). [PubMed: 26559377]
38. Singhi AD, Koay EJ, Chari ST & Maitra A. Early Detection of Pancreatic Cancer: Opportunities and Challenges. Gastroenterology 156, 2024–2040 (2019). [PubMed: 30721664]
39. Hruban RH, Maitra A. & Goggins M. Update on Pancreatic Intraepithelial Neoplasia. Int. J. Clin. Exp. Pathol. 1, 306 (2008). [PubMed: 18787611]
40. Canto MI et al. Screening for Early Pancreatic Neoplasia in High-Risk Individuals: A Prospective Controlled Study. Clin. Gastroenterol. Hepatol. 4, 766–781 (2006). [PubMed: 16682259]
41. Zhu L, Shi G, Schmidt CM, Hruban RH & Konieczny SF Acinar Cells Contribute to the Molecular Heterogeneity of Pancreatic Intraepithelial Neoplasia. Am. J. Pathol. 171, 263–273 (2007). [PubMed: 17591971]
42. Morris IV JP, Cano DA, Sekine S, Wang SC & Hebrok M. β-catenin blocks Kras-dependent reprogramming of acini into pancreatic cancer precursor lesions in mice. J. Clin. Invest. 120, 508–520 (2010). [PubMed: 20071774]
43. Messal HA et al. Tissue curvature and apicobasal mechanical tension imbalance instruct cancer morphogenesis. Nat. 2019 5667742 566, 126–130 (2019).
44. Xu S. et al. The role of collagen in cancer: from bench to bedside. J. Transl. Med. 2019 171 17, 1–22 (2019).
45. Puls TJ, Tan X, Whittington CF & Voytik-Harbin SL 3D collagen fibrillar microstructure guides pancreatic cancer cell phenotype and serves as a critical design parameter for phenotypic models of EMT. PLoS One 12, e0188870 (2017).
46. Drifka CR et al. Highly aligned stromal collagen is a negative prognostic factor following pancreatic ductal adenocarcinoma resection. Oncotarget 7, 76197 (2016). [PubMed: 27776346]
47. Drifka CR et al. Periductal stromal collagen topology of pancreatic ductal adenocarcinoma differs from that of normal and chronic pancreatitis. Mod. Pathol. 2015 2811 28, 1470–1480 (2015).
48. Sunderland SS The anatomy and physiology of nerve injury. Muscle Nerve 13, 771–784 (1990). [PubMed: 2233864]
49. Lundborg G. & Dahlin LB Anatomy, Function, And Pathophysiology Of Peripheral Nerves And Nerve Compression. Hand Clin. 12, 185–193 (1996). [PubMed: 8724572]
50. Axer H, Axerl M, Krings T. & Keyserlingk DG v. Quantitative estimation of 3-D fiber course in gross histological sections of the human brain using polarized light. J. Neurosci. Methods 105, 121–131 (2001). [PubMed: 11275269]
51. Fraley SI et al. Three-dimensional matrix fiber alignment modulates cell migration and MT1-MMP utility by spatially and temporally directing protrusions. Sci. Reports 2015 51 5, 1–13 (2015).
52. Rios AC et al. Intraclonal Plasticity in Mammary Tumors Revealed through Large-Scale Single-Cell Resolution 3D Imaging. Cancer Cell 35, 618–632.e6 (2019). [PubMed: 30930118]
53. Cuccarese MF et al. Heterogeneity of macrophage infiltration and therapeutic response in lung carcinoma revealed by 3D organ imaging. Nat. Commun. 2017 81 8, 1–10 (2017).
54. Saltz J. et al. Spatial Organization and Molecular Correlation of Tumor-Infiltrating Lymphocytes Using Deep Learning on Pathology Images. Cell Rep. 23, 181–193.e7 (2018). [PubMed: 29617659]
55. Lehmann BD et al. Refinement of Triple-Negative Breast Cancer Molecular Subtypes: Implications for Neoadjuvant Chemotherapy Selection. PLoS One 11, e0157368 (2016).
56. Nirschl JJ et al. A deep-learning classifier identifies patients with clinical heart failure using whole-slide images of H&E tissue. PLoS One 13, e0192726 (2018).

Online Methods References:

1. Goode A, Gilbert B, Harkes J, Jukic D, Satyanarayanan M, OpenSlide: A vendor-neutral software foundation for digital pathology. Journal of pathology informatics 4, 27 (2013). [PubMed: 24244884]
2. Kartasalo K. et al. Comparative analysis of tissue reconstruction algorithms for 3D histology. Bioinformatics 34, 3013 (2018). [PubMed: 29684099]
3. Wu PH et al. High-throughput ballistic injection nanorheology to measure cell mechanics. Nat. Protoc. 2012 71 7, 155–170 (2012).
4. Graham S. et al. Hover-Net: Simultaneous segmentation and classification of nuclei in multi-tissue histology images. Med. Image Anal. 58, 101563 (2019).
5. Bankhead P. et al. QuPath: Open source software for digital pathology image analysis. Sci. Reports 2017 71 7, 1–7 (2017).
6. Falkena W, xml2struct. (2020).
7. Fraley SI et al. Three-dimensional matrix fiber alignment modulates cell migration and MT1-MMP utility by spatially and temporally directing protrusions. Sci. Reports 2015 51 5, 1–13 (2015).
8. Hoffmann H, Simple violin plot using matlab default kernel density estimation. INRES (University of Bonn), (2015).

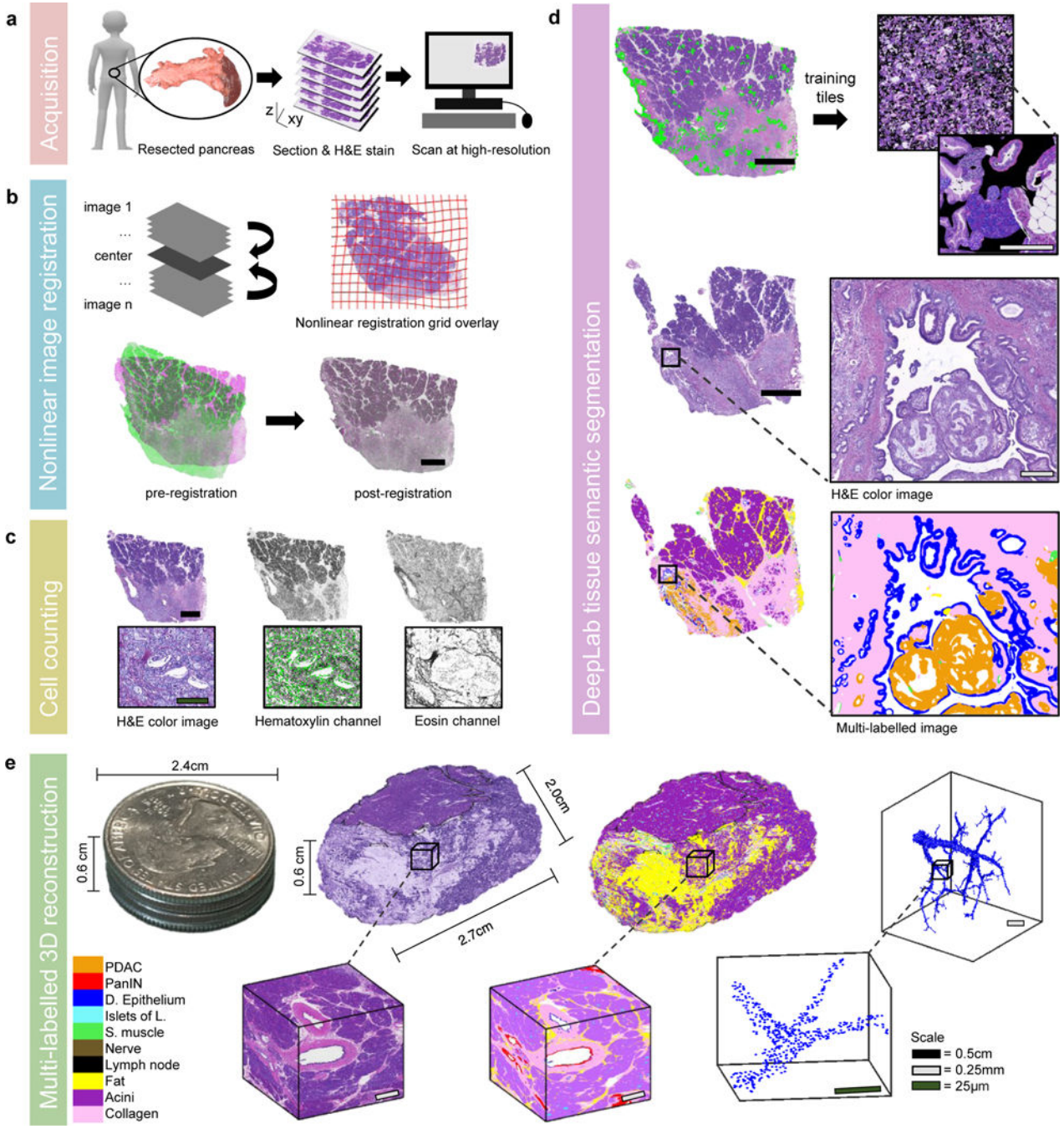

Fig. 1. CODA.

(**a**) Human pancreatic tissue was serially-sectioned, stained, and scanned. (**b**) Images were registered using a nonlinear approach to create a digital volume. (**c**) Cells were identified using the hematoxylin channel of the H&E images. (**d**) Deep learning semantic segmentation models were trained using randomly overlaid annotations of tissue types. Images are labelled to a resolution of 2µm. (**e**) 3D reconstruction of >1000 serially sectioned pancreas sections. 3D renderings are created at the cm, mm, and µm scale at tissue and single cell resolution.

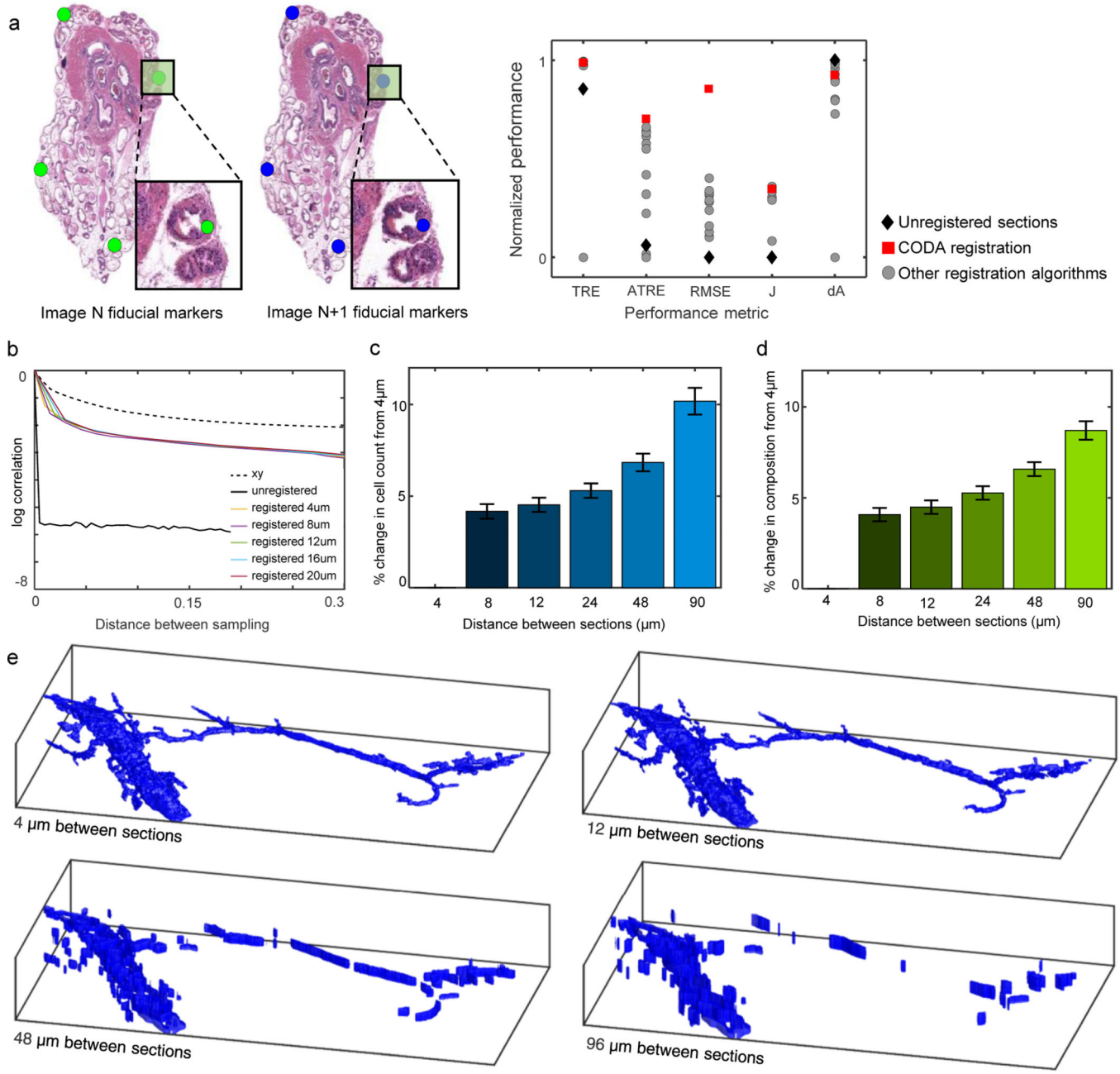

Fig. 2. Validation of CODA registration and ability to skip z-sections.

(**a**) Sample validation image (from an online dataset first published in ref [34]) with overlayed fiducial points. Normalized performance metrics: target registration error (TRE); accumulated target registration error (ATRE); root mean squared error (RMSE); Jaccard Index (J); and pre/post registration change in area (dA). (**b**) Quantification of loss in quality due to reducing the z-resolution of serial samples. Calculation of pixel correlation across the z-axis (left) shows that >95% correlation is maintained post-registration when skipping up to four serial sections, or 20µm, between each H&E collected. (**c**) Calculation of % change in cell count and (**d**) tissue composition (right) reveals <5% error in 3D cell count and tissue

composition extrapolation when skipping up to two serial sections, or 12μm, between each H&E collected). (**e**) Validation of 3D rendering quality due to reducing the z-resolution of serial samples. Tissues in this study are modeled using a spacing of 12 μm between sections (top-right rendering).

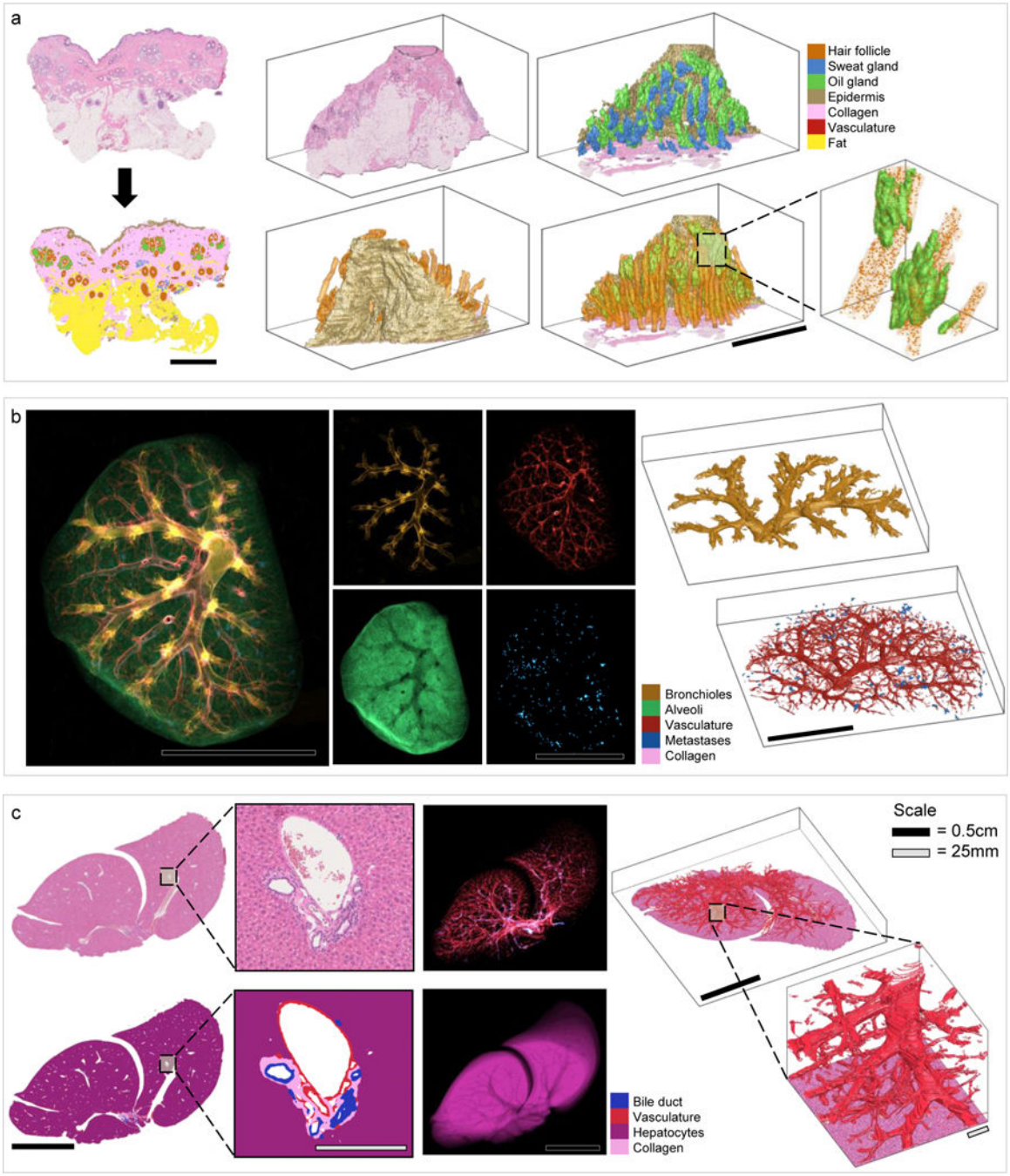

Fig. 3. CODA processing of additional organs.

(**a**) 3D reconstruction of human scalp tissue. Sample H&E and semantically segmented image (far left), visualization of the H&E volume (topleft), epidermis, sweat glands, and oil glands (top right), external (bottom left) and internal (bottom right) views of epidermis, hair follicles and oil glands, and visualization of single cell resolution (far right). (**b**) 3D reconstruction of mouse lung tissue. Z-projections of all components together and individually (left) and 3D renderings of bronchioles (right-top) and vasculature and metastases (right-bottom). (**c**) 3D reconstruction of mouse liver tissue. Sample H&E and

semantically segmented image (far left), z-projection of vasculature and bile duct (middle-top) and hepatocytes (middle-bottom) and 3D rendering of vasculature (far right).

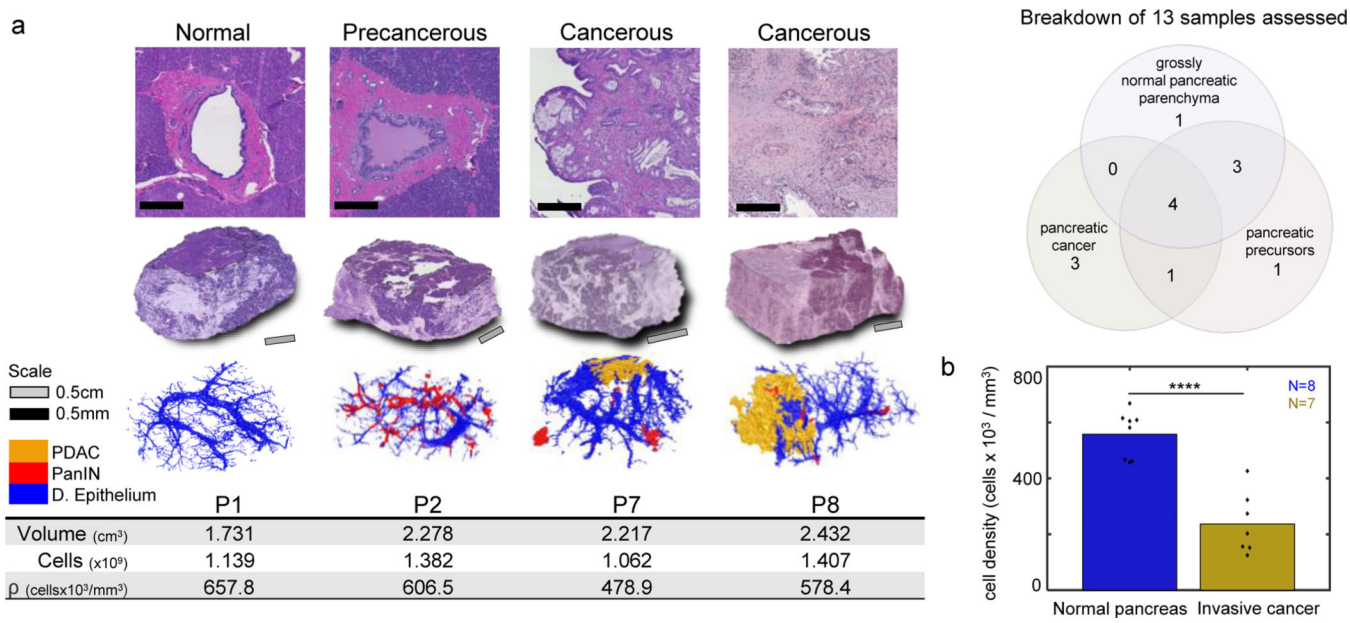

	P1	P2	P7	P8
Volume (cm³)	1.731	2.278	2.217	2.432
Cells (x10⁹)	1.139	1.382	1.062	1.407
ρ (cellsx10³/mm³)	657.8	606.5	478.9	578.4

Fig. 4. Inter-patient pancreas analysis from cm-scale to single cell resolution.

(**a**) Thirteen samples of up to multi cm-scale containing normal, precancerous, and cancerous human pancreas were reconstructed. Tissue volumes, cell counts, and cell densities were calculated. (**b**) Bulk cell density decreases > 3-fold in N=7 cancerous human pancreas relative to N=8 grossly normal human pancreas. **** indicates a p-value<0.0001 using the Wilcoxon rank sum test.

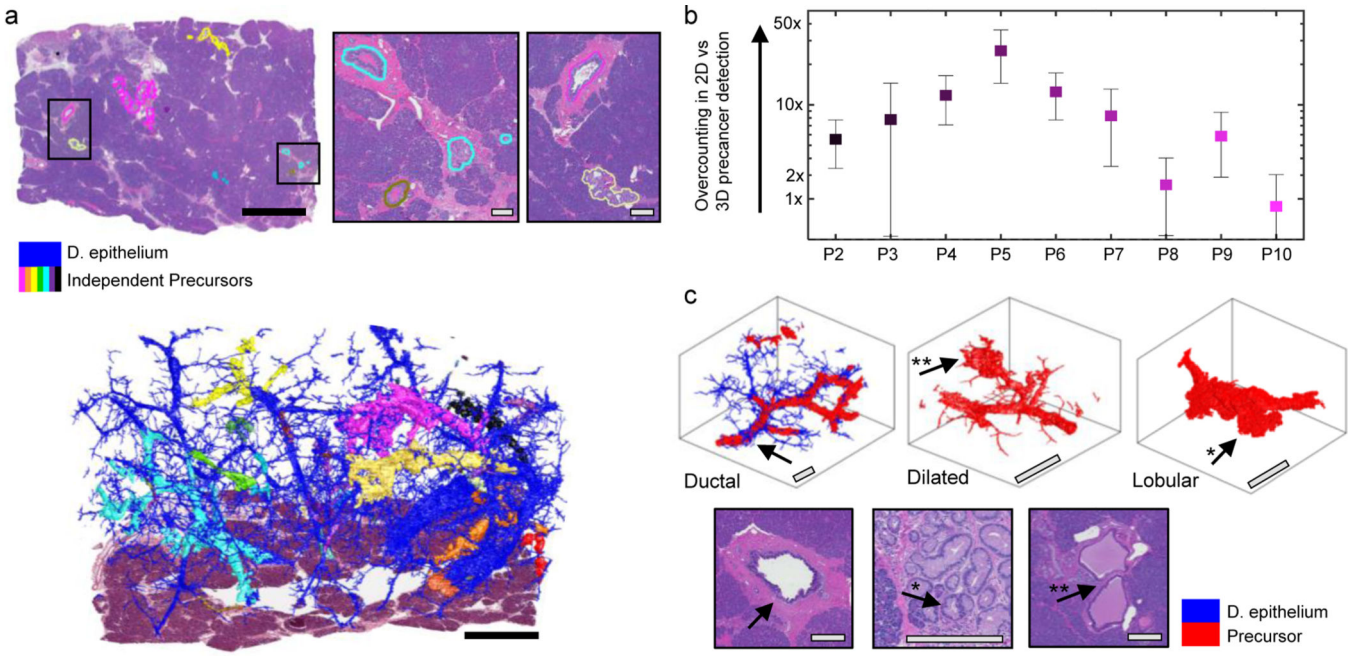

Fig. 5. Microarchitectural patterns in pancreatic precancers.

(**a**) 43 Spatially independent precancers in sample P2 were color coded and labelled on H&E serial sections and a 3D reconstruction. (**b**) Number of precancers per 2D section normalized by true 3D precancer number was calculated for samples containing precancers. (**c**) 3D renderings and sample histology illustrate three 3D phenotypes of PanIN observed. Tubular PanIN preserve normal pancreatic ductal morphology, lobular PanIN resemble acinar lobules, and dilated PanIN reside in dilated ducts or lobules.

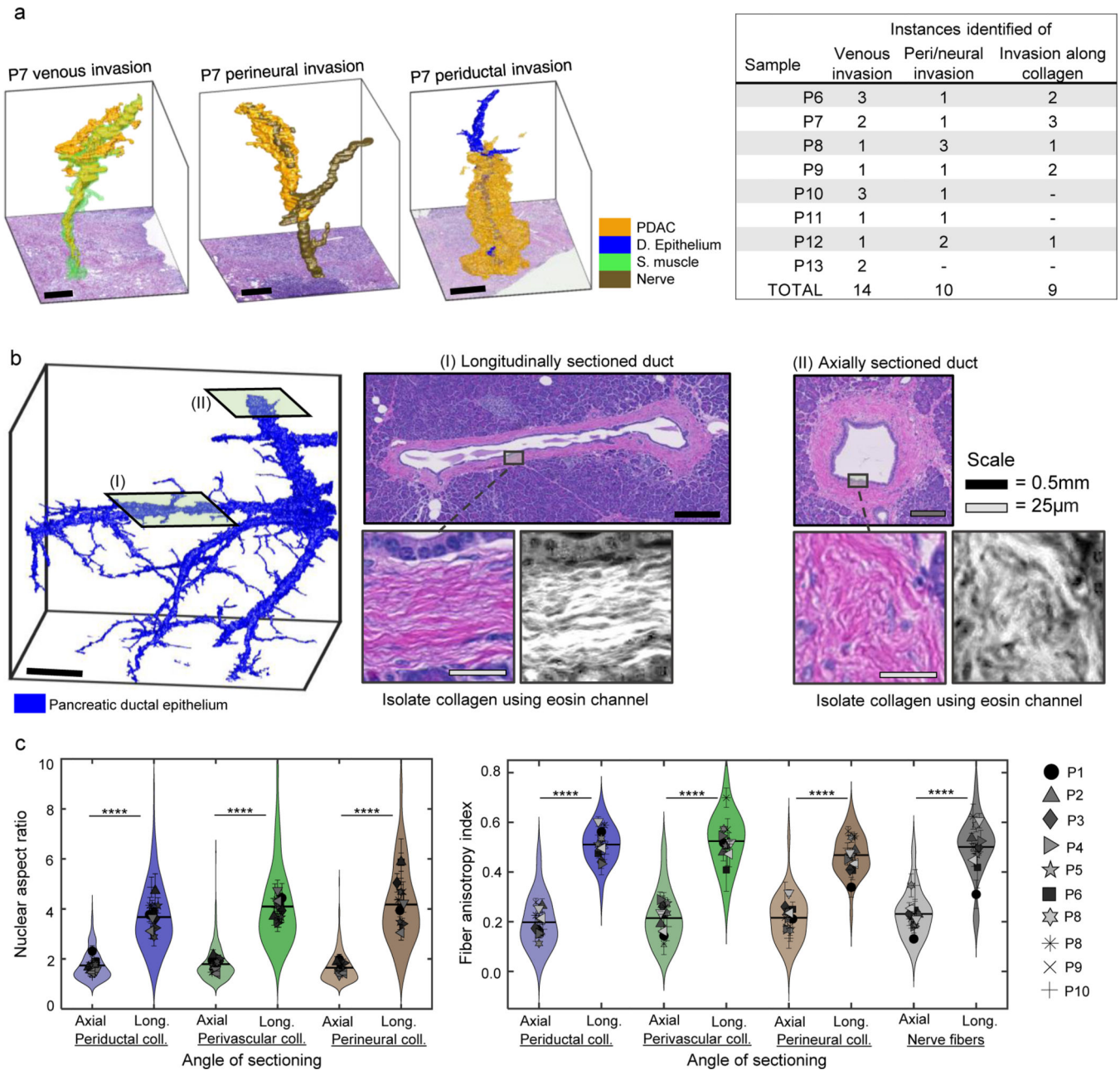

Sample	Instances identified of Venous invasion	Peri/neural invasion	Invasion along collagen
P6	3	1	2
P7	2	1	3
P8	1	3	1
P9	1	1	2
P10	3	1	-
P11	1	1	-
P12	1	2	1
P13	2	-	-
TOTAL	14	10	9

Fig. 6. 3D Patterns in pancreatic cancer invasion.

(**a**) Occurrence of venous invasion, (peri)neural invasion, and invasion along collagen fibers identified in eight samples containing PDAC. Selected 3D reconstructions of pancreatic cancer invasion patterns: invasion along periductal collagen, venous invasion, and perineural invasion. (**b**) 3D reconstruction of normal ductal epithelium with identified coordinates of longitudinal and axial sectioning. H&E images extracted from coordinates and eosin channel isolated. (**c**) Nuclear aspect ratio and fiber anisotropy index, representing local fiber alignment, of 90 longitudinally and 90 axially sectioned ducts, blood vessels, and nerves from 10 patient samples. Nuclear elongation and fiber alignment were significantly higher

in longitudinal compared to axial sections. **** indicates a p-value < 0.0001 using the Wilcoxon rank sum test.